ACS APPLIED MATERIALS & INTERFACES

www.acsami.org Research Article

Engineering a Self-Delivery Nanoplatform for Chemo-Photodynamic-Immune Synergistic Therapies against Aggressive Melanoma

Fei Wu, Xianquan Feng, Wenhao Gao, Lingjun Zeng, Bingbing Xu, Zhenzhen Chen, Changqing Zheng, Xiaomu Hu, Shiying Xu, Hongtao Song,* Xin Zhou,* and Zhihong Liu*

Cite This: https://doi.org/10.1021/acsami.4c18469 Read Online

ACCESS | Metrics & More | Article Recommendations | Supporting Information

ABSTRACT: The effectiveness of immunotherapy in killing melanoma is hindered by a T-cell deficiency and the lack of tumor immunogenicity. Consequently, there is an urgent need for a platform that can further activate the immune system and boost the immune response of the host to tumors. Compared with monotherapy, combination therapy shows promise in improving treatment efficacy and response rates. This study introduces the pioneering use of a rationally designed active targeting nanoplatform to bind axitinib, paclitaxel, and verteporfin to human serum albumin (APV@HSA NPs). APV@HSA NPs have demonstrated the capability to induce dual-induced apoptosis in tumor cells through chemo- and photodynamic effects, while also enhancing immunogenic cell death and promoting dendritic cell maturation. Additionally, the platform promoted the production of $CD8^+$ T cells and memory T cells and inhibited vascular endothelial growth factor via axitinib, facilitating the infiltration of immune effector cells and optimizing chemo-photodynamic immunotherapy. Hence, amplified chemo-photodynamic-immunological nanomedicines with excellent biocompatibility have been redesigned to inhibit the tumor microenvironment and combat the growth of primary tumor and lung metastasis. This approach initiates a series of immune responses, presenting a promising therapeutic strategy for melanoma.

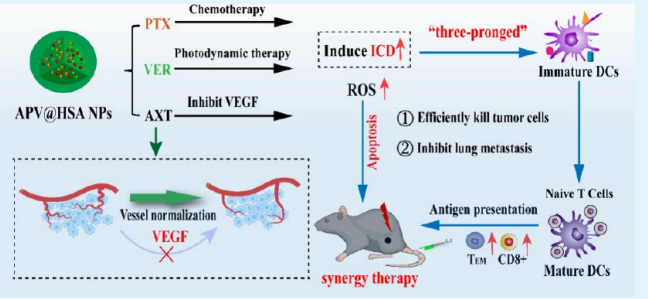

KEYWORDS: *melanoma, chemotherapy, photodynamic therapy, immunogenic cell death, vascular endothelial growth factor*

1. INTRODUCTION

Melanoma is a highly malignant tumor known for its propensity to metastasize, poor clinical prognosis, and high mortality rate. Regarded as one of the most aggressive malignancies in human, it exerts a profound impact on the lives and health outcomes of individuals it afflicts.[1−4] Once melanoma metastasized, the treatment process becomes significantly more intricate. The current treatments for metastatic melanoma have not been successful.[5] Chemotherapy is the primary treatment for metastatic melanoma, with studies indicating that only 10 to 15% of patients respond well, and the 5-year survival rate ranges from 2 to 6%.[6] Consequently, chemotherapy's effectiveness in treating metastatic melanoma is limited. Thus, it is imperative to explore an innovative approach that can enhance the efficacy and safety of the treatment.

The development of tumor is intricately related to the surveillance of the body's immune system. Immunotherapy shows promise in regulating the tumor microenvironment and activating the body's immune system by utilizing antigens, cytokines, and other foreign agents. This approach aims to impede and eradicate tumors, presenting a novel and potentially effective strategy for clinical tumor treatment.[7−9] Furthermore, inducing immunogenic cell death (ICD) represents an innovative method in tumor immunotherapy, focusing on enhancing the immunogenic properties of deceased tumor cells.[10] ICD is a form of tumor cell death that triggers an antitumor immune response.[11,12] It can release danger-associated molecular patterns (DAMPs), such as calreticulin (CRT), high mobility group protein B1 (HMGB1), and adenosine triphosphate (ATP). These DAMPs activate the host immune system against tumors by promoting the maturation of dendritic cells and T lymphocyte proliferation, thereby inducing specific immune responses and establishing durable antitumor immunity.[13]

Studies have indicated that specific chemotherapy drugs, such as anthracyclines and taxanes, not only prompt apoptosis

Received: October 25, 2024
Revised: February 7, 2025
Accepted: February 7, 2025

https://doi.org/10.1021/acsami.4c18469
ACS Appl. Mater. Interfaces XXXX, XXX, XXX−XXX

Scheme 1. Preparation Process of APV@HSA NPs and Its Chemo-Photodynamic-Immunotherapy Diagram for Melanoma

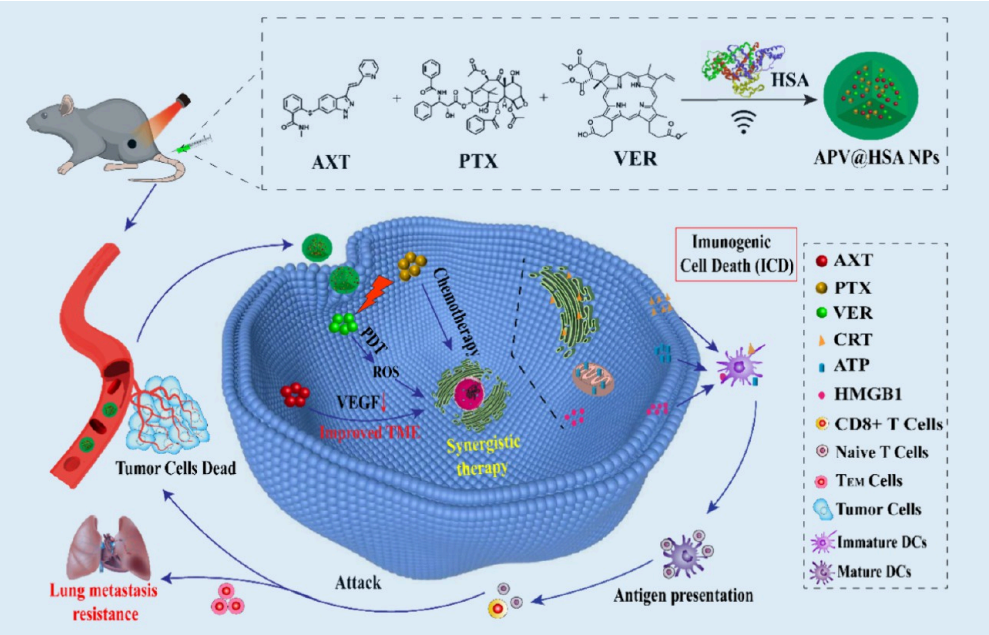

in tumor cells but also trigger ICD, activating the immune system.[14] Paclitaxel (PTX) is a naturally occurring anticancer drug commonly employed in the treatment of various solid tumors, including breast cancer[15] and melanoma.[16,17] Relevant evidence suggests that PTX has the ability to enhance tumor suppression by inducing ICD in tumor cells and subsequently activating dendritic cells.[18] In view of the extensive utilization of PTX in melanoma immunotherapy, PTX has been selected as an ICD inducer. Combination strategies have demonstrated superior therapeutic outcomes when compared to induced ICD through single-chemotherapy regimens. Multimodal therapy not only reduces the systemic toxicity with monotherapy but also remodels the tumor microenvironment, thereby effectively enhancing tumor response.[19] Recent studies confirm the potential benefits of utilizing combined chemotherapy and other treatments in inducing ICD.[20] Consequently, chemotherapy-based combination therapies have garnered significant research attention. For example, chemo-photodynamic combination therapy,[21] chemo-immunization combination therapy,[22] and the innovative approach of combining three therapies: chemo-photothermal-photodynamic combination therapy.[23]

Photodynamic therapy (PDT) involves the use of specific wavelengths to activate photosensitizers (PS) that have accumulated at the tumor site.[24] This activation causes the PS to produce cytotoxic reactive oxygen species (ROS),[25] leading to apoptosis through strong oxidation. On the other hand, PDT-induced ICD stimulates the release of tumor-associated antigens (TAAs) from tumor cells, which subsequently triggers the maturation of dendritic cells and activates the immune response.[26,27] Due to its minimally invasive characteristics, low systemic toxicity, and favorable side effect profile, PDT has emerged as a widely utilized treatment for increasing array of oncologic and nononcologic indications.[28−30] Studies have demonstrated that the depth of light penetration into tissues is positively correlated with longer wavelengths.[31] Among the approved second-generation PS, verteporfin (VER) has a long-wavelength near-infrared light absorption (approximately 690 nm), enabling enhanced tissue penetration. Therefore, VER was chosen as the inducer of ICD in the present study. The combination of PTX-mediated chemotherapy and VER-enhanced PDT is expected to synergistically induce the tumor ICD.

Studies indicate that tumor cells continuously secrete overabundant amounts of vascular endothelial growth factor (VEGF), resulting in an excessive release of pro-angiogenic factors and rapid formation of abnormal vasculature.[32,33] The abnormal vasculature also hinders the deep infiltration of immune cells into the tumor tissue,[34] thus facilitating the immune escape of tumor cells.[35] Meanwhile, studies have shown that VEGF not only enhances the proliferation of immunosuppressive cells, such as tumor-associated macrophages (TAMs) and regulatory T cells (Tregs),[36,37] but also suppresses maturation of dendritic cells and the function of T lymphocytes.[38,39] Consequently, this undermines the approach of concurrently inducing ICD through PTX-based chemotherapy, and PDT mediated by VER is impeded by the tumor microenvironment. In light of this, it is essential to reverse the immunosuppressive effect of VEGF to boost the effectiveness of chemo-photodynamic immunotherapy for melanoma by ameliorating the tumor's immunosuppressive surroundings. Axitinib (AXT) is a robust and markedly selective tyrosine kinase inhibitor targeting the vascular endothelial growth factor receptor (VEGFR).[40,41] Recent studies have shown that AXT facilitates the infiltration of immune effector cells into tumors and reverses the immunosuppressive effects of VEGF. Consequently, this results in a more favorable immunosuppressive microenvironment and improved tumor immunotherapy.[42]

Taking into account the aforementioned evidence, we proposed an integrated chemo-photodynamic-immunological approach for melanoma treatment. However, the untargeted delivery of AXT, PTX, and VER results in low tumor concentrations. The aim of this proposition is to devise a nano drug delivery system to address these challenges. Human serum albumin (HSA) serves as a primary circulating

https://doi.org/10.1021/acsami.4c18469
ACS Appl. Mater. Interfaces XXXX, XXX, XXX−XXX

transporter protein in the human body, displaying superior drug affinity compared to other transporters.[43] It has been demonstrated that employing HSA as a drug carrier in nanoparticles significantly improves both the tumor-targeting efficacy and biocompatibility of the nanoparticles.[44] Considering these factors, HSA has been recognized as the optimal carrier for the nanodrug delivery system in this study.

The aim of this study is to create a nanoparticle formulation (APV@HSA NPs) that integrates to reshape the immunosuppressive tumor microenvironment (as illustrated in Scheme 1). After the intravenous injection of APV@HSA NPs into mice with tumors, the nanoparticles specifically targeted tumor tissues through albumin's active interactions with its receptors gp60 and secreted protein acidic and rich in cysteine (SPARC), along with the enhanced permeability and retention (EPR) effect. Consequently, there is a significant increase in the accumulation of therapeutic agents at the lesion site. The chemotherapeutic agent PTX induces apoptosis and triggers ICD, releasing DAMPs such as CRT, ATP, and HMGB1. These DAMPs contribute to the increased immunogenicity of tumor cells. Additionally, VER upon exposure to 635 nm laser irradiation generates ROS, which can also induce ICD due to their powerful oxidative properties. Under the combined influence of chemo-PDT, the DAMPs can be released and internalized by dendritic cells. This process leads to the maturation and differentiation of dendritic cells, enabling them to present antigens to T lymphocytes and thus triggering the body's immune response. Additionally, the release of AXT at the tumor site has been demonstrated to inhibit the activity of VEGF, counteracting its immunosuppressive effects, which can promote the infiltration of immune effector cells into the tumor and improves the immunosuppressive microenvironment, ultimately enhancing immunotherapy for melanoma. These strategies present a new avenue for stimulating the body's antimelanoma immune response.

2. EXPERIMENTAL SECTION

2.1. Materials. AXT (99%) was sourced from Macklin, PTX (99%) was supplied by Aladdin, VER (98%) was purchased from USP, and HSA (96−99%) was provided by Yuanye. The ultrafiltration tube with a molecular weight cutoff of 30 kDa was obtained from Merck. Methylthiazolyldiphenyl tetrazolium bromide (MTT) was supplied by Aladdin. RMPI 1640 medium with penicillin−streptomycin (RPMI 1640 + 10%FBS), phosphate-buffered saline (PBS), and 4′,6-diamidino-2-phenylindole (DAPI) were purchased from KeyGEN BioTECH Co., Ltd. (China). Fetal bovine serum (FBS) was obtained from PAN Seratech (Germany). Monoclonal antibodies to CD45-PerCP-Cy5.5, CD44L-PE-Cy7, CD80-PE, CD86-APC, CD3-PE, CD11b-FITC, CD8-FITC, and CD11c-PE-Cy7 were purchased from BD Biosciences (USA). The monoclonal antibodies of MHC-II-PE-Cy7 and CD62L-BV421 were supplied from BioLegend (USA).

2.2. Cells and Animals. B16F10 cells (mouse melanoma) and L929 cells (mouse fibroblast) were obtained from Shanghai Cell Bank, Chinese Academy of Sciencesm and cultured in RPMI 1640 + 10%FBS.

C57BL/6 male mice (18−20 g), approximately 7 weeks old, were procured from Shanghai Slack Laboratory Animal Co., Ltd. The mouse melanoma model was established by subcutaneously inoculating 1×10^6 B16F10 cells into the right buttocks of the mice. Once the tumor volume reached approximately 50−100 mm^3, the mice were divided into different experimental groups. Animal experiments were conducted in accordance with the Regulations of the State Science and Technology Commission of the People's Republic of China on the Administration of Laboratory Animals and were approved by the Experimental Animal Ethics Committee of the 900th Hospital of Joint Logistic Support Force, PLA.

2.3. Preparation of APV@HSA NPs. APV@HSA NPs were synthesized using an ultrasonic method. The cytotoxicity of the free drugs toward B16F10 cells was assessed through the MTT assay to determine the optimal ratio of AXT, PTX, and VER. Compusyn software was employed to calculate the combination index (CI) value (CI < 1 indicated synergistic effects; CI = 1 showed additive action; and CI > 1 suggested antagonistic action), aiding in identifying the most effective drug ratio. The optimized procedure involved dissolving AXT, PTX, and VER in DMSO separately; combining AXT (400 μg), PTX (150 μg), and VER (200 μg) solutions mixed as the organic phase; and dissolving HSA (20 mg) in ultrapure water (4 mL) as the aqueous phase. The organic phase was added to the aqueous phase, followed by ultrasonication at 400 W for 20 min to obtain the APV@HSA NP solution. The supernatant was then transferred to an ultrafiltration tube (MWCO = 30 kDa) and washed with 0.9% NaCl through ultrafiltration five times to eliminate the DMSO solvent, free AXT, PTX, and VER. The preparation steps for AXT@HSA NPs, PTX@HSA NPs, and VER@HSA NPs mirrored the above procedure.

2.4. The Characteristics of APV@HSA NPs. The morphology of the nanoparticles was examined by transmission electron microscopy (TEM). The size and zeta potential of the nanoparticles were measured using dynamic laser scattering (DLS) with the Litesizer 500, from Austria. The drug loading of APV@HSA NPs was assessed through UV−vis absorption, infrared, and fluorescence spectroscopy. The excitation/emission (Ex/Em) wavelengths of VER are 435 nm/700 nm, respectively. The crystalline phase states of AXT, PTX, and VER within APV@HSA NPs were explored by X-ray diffraction (XRD) and differential scanning calorimetry (DSC). Encapsulation efficiency (EE) of AXT, PTX, and VER was determined via high-performance liquid chromatography (HPLC), where EE = quality of drug loaded in APV@HSA NPs/quality of the initial drugs input × 100%. We centrifuged and ultrafiltered (MWCO = 30 kDa) the APV@HSA NPs to remove the free drug. The purified APV@HSA NPs underwent freeze-drying to assess the drug loading. The loading content was then assessed using the following equation: drug loading content (DLC) (%) = (weight of loaded drugs)/(weight of nanoparticles) × 100%.

2.5. *In Vitro* Stability. The stability of APV@HSA NPs in aqueous solution, PBS, and RPMI 1640 + 10%FBS was investigated. The nanoparticles were stored at room temperature for 7 days, with their particle size and PDI monitored over time to assess the stability. To assess the effectiveness of laser irradiation stabilization in the nanoparticle solution, a 635 nm laser with an illumination intensity of 350 mW/cm^2 was applied for 10 min. The absorption values of free VER, VER@HSA NP, PTX@HSA NP+VER@HSA NP, and APV@HSA NP solutions were measured at 686 nm.

To enhance stability further, the aqueous nanoparticles were converted into a freeze-dried powder using lactose, maltose, sucrose, trehalose, glucose, and mannitol as freeze-drying protectants. The morphology and visual characteristics of the freeze-dried powder were examined before being redissolved in water. Subsequently, the particle size and PDI were measured and compared to prefreeze-drying samples to assess feasibility.

2.6. Investigation of the Formation Mechanism. To explore the binding forces among AXT, PTX, and VER, the impact of introducing various interaction inhibitors on the dissociation of APV@HSA NPs was investigated. Different concentrations (10, 20, 40, and 80 mmol/L) of urea (hydrogen bonding disruptor), sodium chloride (charge interaction disruptor), Tween 20 (hydrophobic interaction disruptor), and sodium dodecyl sulfate (hydrophobic interaction disruptor) were studied for their effect on nanoparticle dissociation. Particle size variations were analyzed to uncover the specific interactions within the nanoparticles.

Simultaneously, to explore the potential formation mechanism of APV@HSA NPs, molecular dynamics (MD) simulations were conducted using the GROMACS software program.

https://doi.org/10.1021/acsami.4c18469
ACS Appl. Mater. Interfaces XXXX, XXX, XXX−XXX

2.7. *In Vitro* Release Behavior of APV@HSA NPs. Specifically, the purified nanoparticle solution was introduced into PBS buffer at pH levels of 7.4, 6.5, and 5.5, with the release medium containing 0.2% (*w*/*v*) Tween 20. The samples were incubated in a thermostatic shaker, with the temperature maintained at 37 °C and a rotation speed of 100 rpm, under conditions of light avoidance. Sampling was conducted at time intervals of 0.5, 1, 2, 4, 6, 8, 10, 12, 24, and 36 h. The concentrations of AXT, PTX, and VER in the release solutions were quantified using HPLC, and the cumulative release rates of these compounds over a 36 h period were subsequently calculated.

2.8. Hemolysis Experiment of APV@HSA NPs. Hemolysis refers to the rupture and subsequent dissolution of the erythrocytes. Certain pharmaceuticals may induce hemolysis following direct intravenous administration, attributable to the presence of hemolytic agents or physical, chemical, or biological factors. Additionally, some drugs may cause blood cell coagulation postinjection, potentially leading to circulatory dysfunction. Therefore, all injectable formulations and drug preparations with the potential to cause hemolysis should be evaluated through hemolytic assays. Accordingly, the hemolytic properties of APV@HSA NPs were studied and their compatibility with blood was assessed. Pure water was utilized as the positive control, and 0.9% NaCl served as the negative control. The hemolytic effects of various concentrations of APV@HSA NP solution on 2% red blood cell suspension were investigated. The absorbance was determined by measuring the optical density at a wavelength of 540 nm throughout the course of the experiment. The formula for calculating hemolysis (%) is as follows:

$$\text{hemolysis}(\%) = \frac{A_{\text{sample}} - A_0}{A_{100} - A_0} \times 100\%$$

A_{sample} refers to the absorbance of the test group, A_0 represents the absorbance of the negative control group, and A_{100} signifies the absorbance of the positive control group.

2.9. Detection of Extracellular Singlet Oxygen Production. The photodynamic production of singlet oxygen by drug-loaded nanoparticles was assessed by using free VER, VER@HSA NPs, and APV@HSA NPs. DPBF (MedChemExpress, USA) reacts rapidly with singlet oxygen, causing a reduction in its absorption peak at 414 nm and making it a common agent for trapping singlet oxygen in order to measure production levels. The photodynamic efficacy of APV@HSA NPs was initially determined using a UV−vis spectrophotometer to observe changes in the absorption peak at 414 nm following the illumination of a mixed solution of DPBF and nanoparticles.

2.10. Cellular Uptake Assay. The time-dependent effect of APV@HSA NPs was investigated both qualitatively by using inverted fluorescence microscopy and quantitatively by using flow cytometry. The cells were incubated for 1, 2, 4, and 6 h in the presence of VER at a concentration of 1 μg/mL. Subsequently, a solution of DAPI, a nuclear stain for cells, was applied. The cells were subsequently incubated in the dark for 10 min before examination under a fluorescence microscope to evaluate nanoparticle uptake. The Ex/Em wavelengths of VER are 435 nm/700 nm, while those for DAPI are 405 nm/466 nm, respectively.

The variations in cellular drug uptake were assessed by analyzing the uptake levels of free VER, VER@HSA NPs, and APV@HSA NPs by the cells. Following cell plating and adhesion onto the surface, the cells were incubated with free VER, VER@HSA NPs, and APV@HSA NPs for 4 h, with a concentration of VER at 1 μg/mL. DAPI solution was then also added to evaluate the uptake of different formulations under a fluorescent inverted microscope.

2.11. *In Vitro* Cytotoxicity Assay. L929 cells and B16F10 cells were inoculated into 96-well cell culture plates at a density of 5×10^3 cells/well and cultured overnight at 37 °C in a 5% CO_2 atmosphere. Different concentrations of HSA, AXT@HSA NPs, PTX@HSA NPs, VER@HSA NPs, and APV@HSA NPs were applied to assess the dark toxicity of the formulations using the MTT assay.

The cellular phototoxicity of APV@HSA NPs was investigated under 635 nm laser irradiation, as no dark toxicity was observed at this concentration. Following a 4 h incubation period, the cells were exposed to laser and then cultured for 20 h. The MTT assay was used to calculate cell viability. Concurrently, the phototoxicity effects of free VER, VER@HSA NPs, and APV@HSA NPs was compared using the optimal laser power.

2.12. Investigation of Cell Apoptosis. The Annexin V-APC/cyanine/PI apoptosis assay kit (Elabscience Biotechnology Co., Ltd., China) was employed to investigate the apoptosis of B16F10 cells induced by nanoparticles. The cells were categorized into groups Control, AXT@HSA NPs, PTX@HSA NPs, free VER+Laser, VER@HSA NPs+Laser, and APV@HSA NPs+Laser and were then incubated with cells under normoxic conditions for 4 h. Following treatment, the cells underwent laser irradiation. The group subjected to laser irradiation was exposed to a 635 nm wavelength laser with a power density of 1 mW/cm^2 for 10 min, followed by an additional 20 h incubation. Conversely, the nonlaser irradiation group was directly transferred to the incubator containing AXT at 0.888 μg/mL, PTX at 0.24 μg/mL, and VER at 0.5 μg/mL. After 24 h of incubation, both groups were enzymatically digested without EDTA, and the samples were processed as per the kit's instructions before being promptly analyzed using flow cytometry.

2.13. Live/Dead Cell Staining Experiments. Live and dead cells were differentiated through staining comprising propidium iodide (PI) and calcein-acetoxymethyl ester (CAM). The cell plating and treatment procedures followed the protocol employed in the apoptosis experiment. Following incubation, the cells were rinsed with PBS and exposed to a prepared mixed working solution as directed in the staining kit for 30−45 min at room temperature. Subsequently, we underwent three PBS washes before being examined under a fluorescence microscope for imaging.

2.14. Detection of Cell ROS Production. The levels of ROS in the cells were quantified using an ROS detection kit (Merck, Germany). The probe was 2,7-dichloroFluorese-indiacetate (DCFH-DA), which is initially nonfluorescent but can undergo enzymatic hydrolysis into DCFH within the cell. Upon exposure to ROS, DCFH is oxidized, resulting in the formation of DCF. The ROS assay was conducted as follows: cells were seeded in six-well plates at a density of 5×10^5 cells/dish and cultured overnight. The experimental groups included blank control, AXT@HSA NPs, PTX@HSA NPs, free VER +Laser, VER@HSA NPs+Laser, and APV@HSA NPs+Laser, with incubation lasting for 4 h. Following the incubation period, the medium was removed, and the wells were rinsed three times with PBS. Subsequently, 1 mL of DCFH-DA dye at a concentration of 1 μmol/L was added to each well, which were then incubated for 20 min. After incubation, the wells were rinsed three times with PBS. The laser irradiation group was then exposed to laser irradiation with a wavelength of 635 nm and a power density of 1 mW/cm^2 for 10 min, in the presence of AXT (0.888 μg/mL), PTX (0.24 μg/mL), and VER (0.5 μg/mL). Upon completion of the incubation, the wells were rinsed three times with PBS, and the samples were observed and imaged using a fluorescence inverted microscope.

2.15. Antitumor Proliferation Test *In Vitro*. The cell plate clone formation assay is an important technical method used to test items such as cell proliferative capacity, invasiveness, and sensitivity to killing factors. Plate cloning test: following cell adhesion and growth, the experimental groups were defined as follows: Control, AXT@HSA NPs, PTX@HSA NPs, AXT+PTX+VER, APV@HSA NPs, free VER +Laser, VER@HSA NPs+Laser, AXT+PTX+VER+Laser, and APV@HSA NPs+Laser. After incubation for 4 h, the laser irradiation group underwent irradiation using a laser with a wavelength of 635 nm. The power density of the laser was set at 1 mW/cm^2, and postirradiation incubation continued for 20 h following a 10 min exposure. The group without laser irradiation was directly incubated in the incubator (AXT = 0.888 μg/mL, PTX = 0.24 μg/mL, VER = 0.5 μg/mL). The drug was administered on days 0 and 3. After a week, the colonies with more than 50 cells were counted under the microscope (≥50 cells were counted as one colony), and the clone formation rate was computed.

2.16. Determination of Biomarkers of Immunogenic Cell Death. After cell adhesion, the cells were divided into six groups for drug administration: Control, AXT@HSA NPs, PTX@HSA NPs, free

https://doi.org/10.1021/acsami.4c18469
ACS Appl. Mater. Interfaces XXXX, XXX, XXX−XXX

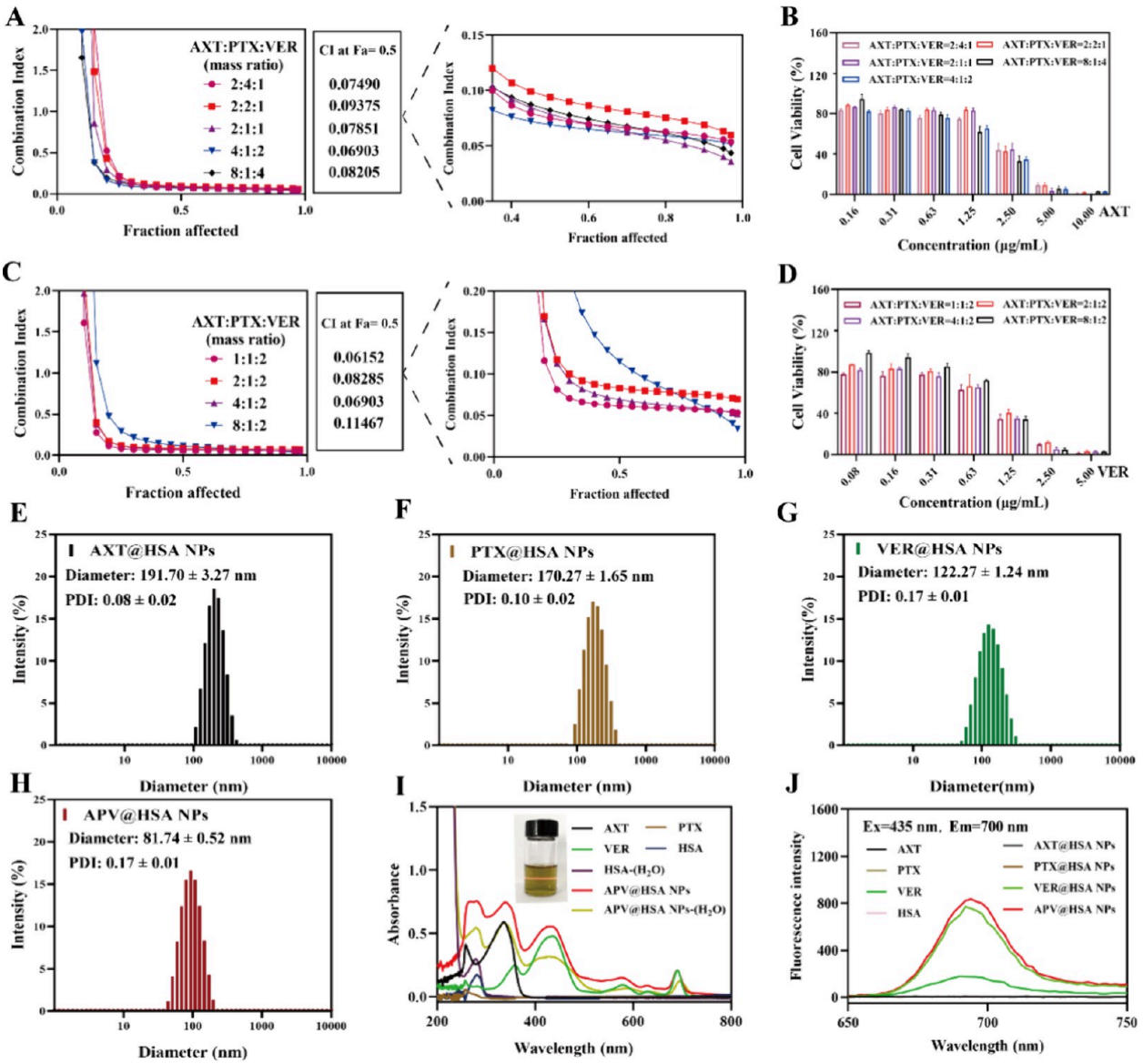

Figure 1. Preparation and characterization of nanoparticles. (A–D) AXT-PTX-VER joint index of different mass ratios and cell survival rate of AXT-PTX-VER with different mass ratios. $n = 6$. (E) Particle size distribution and PDI of AXT@HSA NPs. (F) Particle size distribution and PDI of PTX@HSA NPs. (G) Particle size distribution and PDI of VER@HSA NPs. (H) Particle size distribution and PDI of APV@HSA NPs. (I) UV–vis absorption spectra of AXT, PTX, VER, and HSA, as well as APV@HSA NPs in both DMSO and water solutions, are presented. Additionally, an image of APV@HSA NPs irradiated by a laser is provided. (J) Fluorescence spectra of AXT, PTX, VER, and their albumin nanomaterials as well as APV@HSA NPs in aqueous solution.

VER+Laser, VER@HSA NPs+Laser, and APV@HSA NPs+Laser. Following a 4 h incubation period, the laser irradiation was applied to the specified groups using a 635 nm wavelength and a power density of 1 mW/cm^2 for 10 min. Subsequently, all groups were further incubated for an additional 20 h. The nonlaser irradiation control group was placed directly in the incubator for subsequent analysis.

CRT and HMGB1. Upon completion of the incubation, the culture medium was aspirated, and the cells were washed thrice with PBS. The antibody was then diluted to 1:200 following the Anti-CRT/AF488 antibody dyeing instructions (Bioss, China). Subsequently, the cells were rinsed with PBS, fixed with 4% paraformaldehyde for 10 min, and stained with DAPI for another 10 min. Cell CRT exposure was visualized using a fluorescence microscope. The translocation of HMGB1 from the nucleus to the extracellular matrix was investigated by the same experimental groups and operation. Ex/Em of Anti-CRT/AF 488 were 495 nm/519 nm, Ex/Em of Anti-HMGB1/AF 488 were 495 nm/519 nm, while those for DAPI were 405 nm/466 nm, respectively.

ATP. The ATP bioluminescence detection kit (Beyotime, China) was used following the manufacturer's instructions. After incubation, cells were lysed using the provided lytic solution and centrifuged at 1000 rpm for 3 min, the lower layer cells were collected, and ATP content in the cells was detected following the kit protocol. This process was carried out in triplicate for each experimental group.

2.17. *In Vivo* Biodistribution Analysis. Subcutaneous injection of 1×10^6 B16F10 melanoma cells was carried out in the right buttocks of C57BL/6 mice when the tumor volume approximately reached 100 mm^3. A dosage of 1 mg/kg of VER was administered, and free VER, VER@HSA NPs, and APV@HSA NPs were injected intravenously. Images were captured at 0.5, 1, 2, 4, 6, 8, 10, 12, and 24 h using an *in vivo* imaging system (AniView 100).

2.18. APV@HSA NPs *In Vivo* Pharmacodynamic Evaluation. In the *in vivo* pharmacodynamic evaluation of nanoparticles, C57BL/6 mice were selected as the melanoma animal model. A total of 1×10^6 B16F10 cells were injected into the right buttocks of the mice to the primary tumor model. When the tumor reached approximately 100

https://doi.org/10.1021/acsami.4c18469
ACS Appl. Mater. Interfaces XXXX, XXX, XXX–XXX

mm^3, the mice were divided into nine groups for administration: 0.9% NaCl, AXT@HSA NPs, PTX@HSA NPs, Free VER+Laser, VER@HSA NPs+Laser, PTX@HSA+VER@HSA NPs+Laser, APV@HSA NPs, APV@HSA NPs+Laser, and DTIC (dacarbazine injection, 5 mg/kg[45,46]). Each group consisted of five mice, and we were administered via the tail vein with a dose of VER at 1 mg/kg. After 4 h of administration, the laser irradiation group was irradiated with laser wavelength of 635 nm and a power density of 350 mW/cm^2 for 10 min. The drug was administered on the 6th, 8th, and 10th days of the experiment. Upon completion of the study, the eyeballs were removed to collect blood samples from the mice, along with major organs (heart, liver, spleen, lungs, and kidneys) and tumor tissue. Blood samples were analyzed for different indexes, including alanine aminotransferase (ALT), blood urea nitrogen (BUN), blood creatinine (CRE), and creatine kinase (CK). Paraffin wax was used for embedding and sectionalization, with subsequent treatment of the sections using TUNEL or H&E staining facilitated by end-deoxynucleotide transferase. The impact of nanoparticles on the normal organs of mice were investigated by microscope observation and photography. Single-cell suspensions of inguinal lymph nodes were assessed through a mechanical dissociation method, followed by antibody staining. Flow cytometry was utilized to quantify mature dendritic cells ($MHC\text{-}II^+CD11c^+CD80^+CD86^+$). Additionally, immunohistochemistry was conducted to analyze the presence of CD31 and VEGF, while immunofluorescence staining was used to detect $CD8^+$ and $Foxp3^+$ markers.

2.19. APV@HSA NP Survival Assessment. A total of 54 tumor-bearing mice were included in the study. B16F10 cells (1×10^6) were injected into the right buttocks of the mice to establish the primary tumor model. Once the tumor reached approximately 100 mm^3, the mice were randomly divided into nine groups: 0.9%NaCl, AXT@HSA NPs, PTX@HSA NPs, Free VER+Laser, VER@HSA NPs+Laser, PTX@HSA+VER@HSA NPs+Laser, APV@HSA NPs, APV@HSA NPs+Laser, and DTIC (dacarbazine injection) groups. After 6, 8, and 10 days of administration, the mice underwent laser therapy. Changes in their weights, tumor sizes, and mortalities within 2 months were meticulously observed, recorded, and monitored in real time.

2.20. APV@HSA NP Evaluation of Inhibitory Effect on Lung Metastases. The animal grouping and dosing regimen in this study mirrored those of the *in vivo* pharmacodynamics experiment. On days 5, approximately 1×10^6 B16F10 cells were intravenously injected, followed by drug administration and laser therapy on days 6, 8, and 10. On the 12th day, three mice in each group were killed for the evaluation of the expression of spleen effector memory T cells ($CD45^+CD3^+CD8^+CD44^+CD62L^-$). The remaining mice underwent continuous monitoring. The mice were killed on the 18th day, and the lung tissue was extracted to observe and record the metastatic nodules in lung tumors.

2.21. Statistical Analysis. One-way ANOVA was performed using GraphPad Prism software to identify significant differences among the groups. The data were expressed as the mean ± standard deviation (SD). $*p < 0.05$, $**p < 0.01$, and $***p < 0.001$ were indicated significant differences.

3. RESULTS AND DISCUSSION

3.1. Synthesis and Characterization of APV@HSA NPs. The dark toxicity of AXT, PTX, and VER on B16F10 cells was initially evaluated using the MTT assay, followed by the assessment of VER's phototoxicity (0.5 mW/cm^2, 10 min). VER exhibited no dark toxicity at concentrations below 5 μg/mL (as shown in Figure S1A,B). Consequently, this concentration was employed for subsequent screening experiments (0.5 mW/cm^2, 10 min). The optimal ratio of PTX to VER was investigated while maintaining the AXT concentration at 10 μg/mL. At AXT:PTX:VER = 4:1:2, the Fa value of the CI was minimized at 0.5, indicating the strongest synergistic effect among AXT, PTX, and VER at this proportion (as shown in Figure 1A), supported by the corresponding cell survival rate curve at said concentration (as shown in Figure 1B). Having set the mass ratio of PTX:VER set at 1:2, adjustments were made to the AXT concentration for ongoing screening (as shown in Figure 1C), alongside the associated cell survival rate (as shown in Figure 1D). At AXT:PTX:VER = 1:1:2, the CI yields the lowest Fa value at 0.5. However, the preparations made at this ratio demonstrate reduced encapsulation rates of AXT and PTX. To enhance the efficacy of AXT, a final mass ratio of 4:1:2 for AXT, PTX, and VER was determined and subsequently employed for further research on preparation. According to the specified proportions, HSA served as the carrier, and AXT, PTX, and VER were added for self-assembly. Subsequently, the APV@HSA NPs were obtained following a single-factor investigation. The preparation process of these self-assembled nanoparticles is simple. The distinctive structural characteristics of AXT, PTX, and VER facilitate interactions with albumin, including hydrophobicity, coordination, hydrogen bond, and $\pi-\pi$ stacking. These interactions enhance the combination efficiency between the drugs and the carrier.

DLS results revealed that the particle sizes of AXT@HSA NPs, PTX@HSA NPs, VER@HSA NPs, and APV@HSA NPs were 191.70 ± 3.27 nm (PDI = 0.08 ± 0.02), 170.27 ± 1.65 nm (PDI = 0.10 ± 0.02), 122.27 ± 1.24 nm (PDI = 0.17 ± 0.01), and 81.74 ± 0.52 nm (PDI = 0.17 ± 0.01), respectively. Additionally, the zeta potentials of AXT@HSA NPs, PTX@HSA NPs, VER@HSA NPs, and APV@HSA NPs were −11.57 ± 0.38, −9.04 ± 0.23, −12.90 ± 0.87, and −14.48 ± 0.42 mV (as shown in Figure 1E−H and Figure S1C−F). Respectively, it is noteworthy that the zeta potential of APV@HSA NPs decreased to −14.48 ± 0.42 mV in comparison. This difference could be attributed to the presence of interaction forces among the three drugs, indicating successful loading. TEM analysis revealed that all four nanoparticles had a consistently dispersed spheroidal morphology, closely matching the nanoparticle sizes measured through DLS (as shown in Figure S1G−J). The APV@HSA NPs were further characterized using UV−vis spectroscopy, and the presence of the characteristic UV absorption peaks of AXT, PTX, VER, and HSA in the spectrum confirmed the successful coassembly of APV@HSA NPs. Meanwhile, the dark-green APV@HSA NPs exhibited a clear Tyndall effect under laser irradiation (as shown in Figure 1I). The AXT@HSA NPs, PTX@HSA NPs, and VER@HSA NPs displayed absorption peaks corresponding to the respective drugs and HSA, validating successful loading (as shown in Figure S1K). Compared to VER in a DMSO organic solution, the maximum absorption peak of APV@HSA NPs in an aqueous solution demonstrated a notable "red-shift" phenomenon, along with an increased width of the absorption peak, suggesting the existence of hydrophobic interactions among the nanoparticles. When excited at 435 nm, the photosensitizer displayed a distinct emission peak at 700 nm. Fluorescence spectroscopy revealed that the fluorescence intensity of free VER was lower compared with that of VER@HSA NPs and APV@HSA NPs in aqueous solution. This difference is likely due to the intermolecular filling of the hydrophobic drug into the core of the albumin nanoparticles, leading to the supramolecular binding of VER with HSA, consequently inhibiting the self-interaction of VER within the molecule. The supramolecular assembly suppressed the self-quenching phenomenon of VER within the molecule, thus enhancing its photophysical characteristics (as shown in Figure 1J).[47,48] The fluorescence results obtained in a DMSO solution

https://doi.org/10.1021/acsami.4c18469
ACS Appl. Mater. Interfaces XXXX, XXX, XXX−XXX

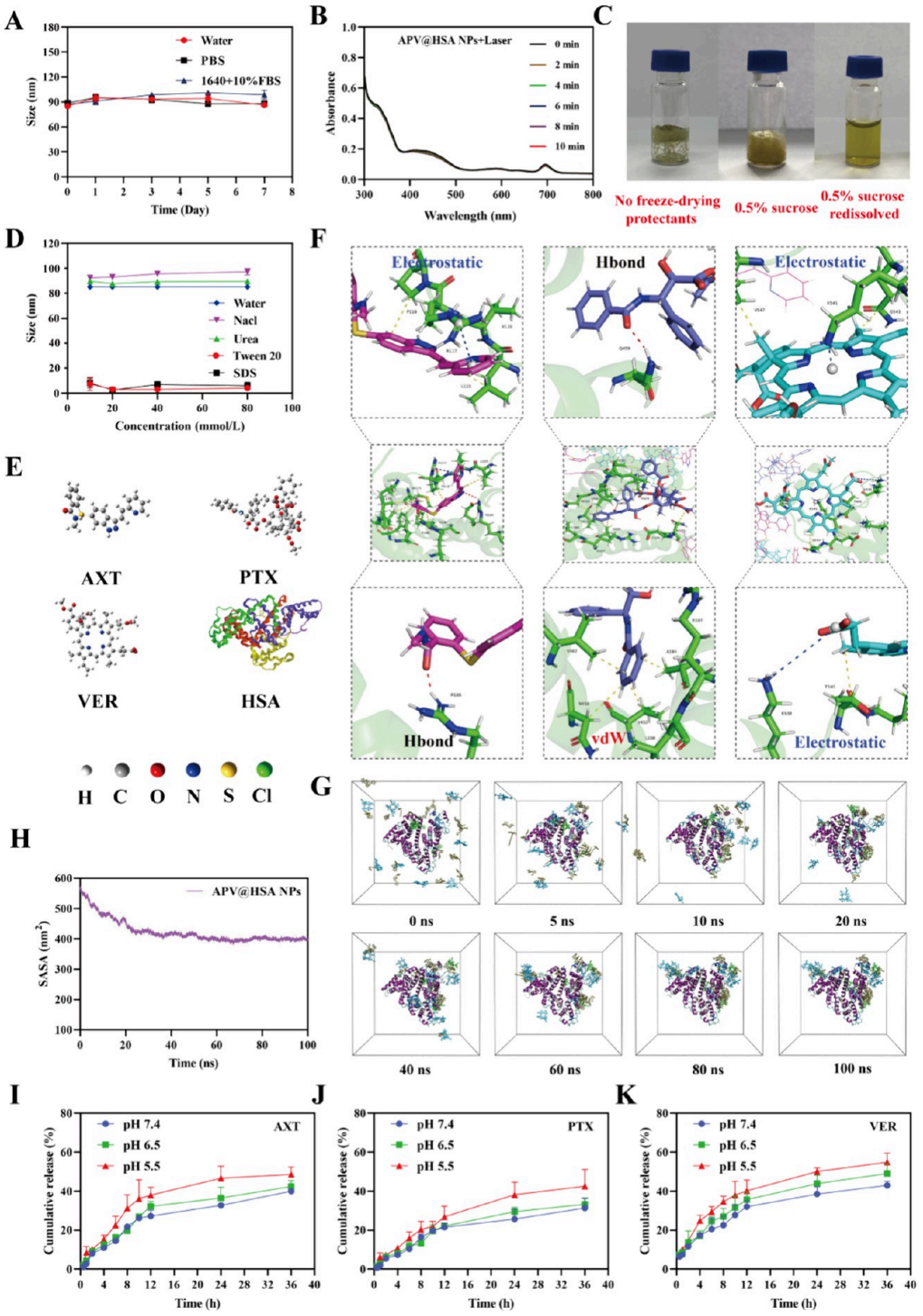

Figure 2. *In vitro* pharmacologic evaluation of APV@HSA NPs. (A) APV@HSA NP stability evaluation of the solution. $n = 3$. (B) Evaluation of laser irradiation stability of APV@HSA NPs. (350 mW/cm^2, 10 min). (C) Freeze-dried nanoparticles without protective agent, freeze-dried nanoparticles with 0.5% sucrose, and redissolved picture. (D) APV@HSA NPs with different concentrations of SDS, polysorbate 20, urea, and sodium chloride change of particle size after incubation. $n = 3$. (E) AXT, PTX, VER, HSA, and related element model diagram. (F) APV@HSA NP interaction force analysis. (G) APV@HSA NP molecular dynamics simulation. (H) APV@HSA NP SASA analysis. (I–K) *In vitro* release of AXT, PTX, and VER from APV@HSA NPs with pH 7.4, 6.5, and 5.5. $n = 3$. Values represented were means ± SD, $^*p < 0.05$, $^{**}p < 0.01$, $^{***}p < 0.001$.

are presented (Figure S1L). The fluorescence imaging results for the drug were consistent with the fluorescence spectroscopy results (as shown in Figure S1M). Further confirmation of the successful coassembly of APV@HSA NPs was provided by the FT-IR spectra, with a slight shift of the absorption peaks attributed to intermolecular hydrophobic interactions also observed in the spectra (as shown in Figure S1N). Following self-assembly, does the physical phase state of a drug change? The AXT, PTX, and VER samples exhibit prominent characteristic diffraction peaks in the range of 5−30°, indicating their crystalline state. In contrast, the APV@HSA NP-lyophilized powder did not exhibit any characteristic

https://doi.org/10.1021/acsami.4c18469
ACS Appl. Mater. Interfaces XXXX, XXX, XXX−XXX

diffraction peaks for AXT, PTX, and VER, indicating that these drugs assumed an amorphous state during the self-assembly process to generate nanoparticles (as shown in Figure S1O). The results of the DSC aligned with those of XRD (as shown in Figure S1P). The optimal encapsulation rate of APV@HSA NPs was determined via HPLC, yielding the following results: AXT = (79.99 ± 0.12) %, PTX = (55.51 ± 0.22) %, and VER = (86.19 ± 0.44) %. The drug loading was calculated as follows: the total drug loading was 2.46%, with AXT = (1.21 ± 0.10) %, PTX = (0.33 ± 0.05) %, and VER = (0.92 ± 0.06) %.

3.2. *In Vitro* Stability. The particle size and PDI of APV@HSA NPs were found to be stable in both deionized water, PBS, and RPMI 1640 + 10% FBS, showing no signs of flocculent precipitation. This indicated that the nanoparticle solution was successfully stabilized for practical applications (as shown in Figure 2A and Figure S2A). The absorbance values of free VER, VER@HSA NP, PTX@HSA NP+VER@HSA NP, and APV@HSA NP solutions at 686 nm remained stable under light intensity conditions of 350 mW/cm^2. A 10 min light exposure suggested favorable photostability of VER in nanoparticle solutions, enabling further cell and animal studies (as shown in Figure 2B and Figure S2B−D). Without a lyophilized protectant, the sample displayed filamentous characteristics, but the particle size remained mostly unchanged after resolubilization. The incorporation of 0.5% sucrose yielded the optimal appearance of the lyophilized powder and resolubilization effect, with minimal impact on particle size compared to other protectants (as shown in Figure 2C, Figure S2E, and Table S1). Among the cryoprotectants, sugars have demonstrated superior cryoprotective abilities compared to polyols, with sugar-based protectants proving more effective in safeguarding nanoparticles during freeze-drying. Sugars are strategically located in nanoparticle crevices before freeze-drying, effectively preventing particle agglomeration until the glass transition temperature. Throughout the drying process, sugars can serve as water molecule substitutes, establishing hydrogen bonds with polar groups on nanoparticle surfaces. Notably, sucrose can crystallize in an amorphous state, and the amorphous morphology of APV@HSA NPs and lyophilization protectants promotes hydrogen bond formation, ensuring superior lyophilization results.

3.3. Investigation of Formation Mechanism. The hydrophobic interactions of the nanoparticles were disrupted by varying different concentrations (10, 20, 40, and 80 mmol/L) of sodium dodecyl sulfate and polysorbate 20. The hydrogen bonding interactions were disrupted by urea, while the charge interactions were disrupted by sodium chloride. The nanoparticles dissociated at low concentrations due to the impact of hydrophobic interaction forces. The introduction of sodium chloride and urea led to a minor change in nanoparticle size, suggesting that the APV@HSA NPs were predominantly bound by hydrophobic interaction forces, supported by charge interaction and hydrogen bonding forces (as shown in Figure 2D). After intermolecular interactions were evaluated, all simulations were performed with Gromacs version 2023.2. The proteins were parametrized using the Amber99SB force field to describe their dynamic characteristics. The models of AXT, PTX, VER, and HSA, including their constituent elements (as shown in Figure 2E). Within the protein system, AXT engaged electrostatic interactions with the arginine amino acids of the protein and established hydrogen bonding interactions with the NH_2 amino group, facilitating AXT binding to the protein. PTX primarily interacted via van der Waals interactions with the hydrophobic amino acids of the protein, forming hydrogen bonding interactions with NH_2 to further stabilize the binding of PTX onto the protein. The central N-containing heterocycle of VER interacts electrostatically with −COO, and van der Waals interactions exist further contributed to stabilizing VER binding to the protein. The binding of AXT, PTX, and VER to HSA not only received structural support but also produced theoretical insights from molecular interaction analysis (as shown in Figure 2F). The results of the MD simulation illustrated that initially, at 0 ns, the drugs exhibited a random distribution within the simulation box. At 5 ns, three distinct drug molecules closely interacted with the protein. Progressing to 10 ns, drug molecules began to aggregate partially. At 20 ns, most of the drug molecules were in contact with the protein. Around 40 ns later, the drug molecules, aggregated, shifted along the protein surface to optimize their configuration and enhance their binding affinity to the protein. Between 80 and 100 ns, each drug molecule was consistently in contact with the protein, firmly docked by the protein (as shown in Figure 2G). The RMSD value indicates the extent of deviation from the average position and serves as a measure of atomic movement magnitude. Analysis revealed significant fluctuations in the RMSD values of individual amino acid residues in the protein system, particularly during the initial stages. These fluctuations were correlated with the transit of drug molecules across the boundary of the simulation box. Ultimately, the RMSD stabilized at 3.81 Å, indicating the establishment of a stable molecular configuration within the system. Interactions among the system components facilitated the formation of the entire structure within 60 ns (Figure S2F). The SASA value quantifies the contact area between molecules and water. A decrease in the SASA value correlates with enhanced molecular association or increased interaction frequency, reflecting the strengthening of intermolecular bonds as the molecules stabilize (as shown in Figure 2H).

3.4. *In Vitro* Release Behavior of APV@HSA NPs. The *in vitro* release results of AXT, PTX, and VER within 36 h are shown, and it can be seen that there was a time and pH dependence of the release of all three drugs. The highest release rates were observed at pH 5.5 with (48.61 ± 3.75%) for AXT, (42.55 ± 4.86%) for PTX, and (54.93 ± 4.62%) for VER. The fastest rate of drug release was observed at pH 5.5. This phenomenon is likely attributable to the unique structural characteristics of AXT, PTX, and VER, wherein the nitrogen-containing groups are susceptible to protonation and are more readily dissociated in acidic environments. This results in the attenuation of the hydrophobic interaction forces within APV@HSA NPs, subsequently inducing their dissociation for drug release. These findings indicate that nanoparticles are more predisposed to dissociate and release therapeutic agents within the tumor microenvironment, possessing specific TME-responsive characteristics that are essential for their antitumor efficacy (as shown in Figure 2I−K).

3.5. Hemolysis Experiment of APV@HSA NPs. The test demonstrated that with an increase in the concentration of the nanoparticle solution, the hemolysis rate gradually rose, indicating a concentration-dependent phenomenon. At a high concentration of VER = 40 μg/mL for 3 h at 37 °C, the hemolysis rate of the nanoparticle solution stayed below 5%. This indicates good compatibility of the nanoparticles with blood, a favorable safety profile, and meeting the requirements for intravenous drug delivery (as shown in Figure S2G,H).

https://doi.org/10.1021/acsami.4c18469
ACS Appl. Mater. Interfaces XXXX, XXX, XXX−XXX

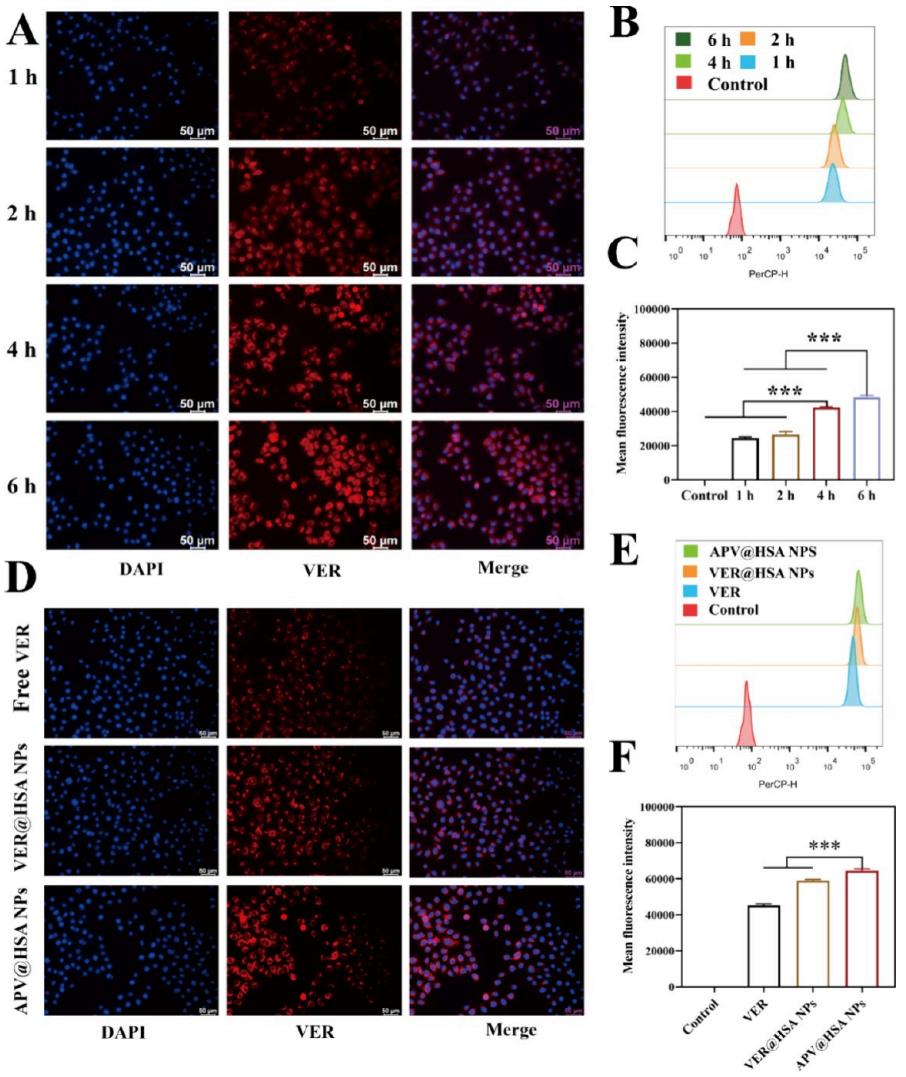

Figure 3. Cell uptake. (A) Uptake of APV@HSA NPs by B16F10 cells at 1, 2, 4, and 6 h by fluorescence microscopy and (B, C) flow cytometry. n = 3. Scale bar: 50 μm. (D) Uptake of free VER, VER@HSA NPs, and APV@HSA NPs by B16F10 cells at 4 h by fluorescence microscope and (E, F) flow cytometry. n = 3. Scale bar: 50 μm.

3.6. Detection of Extracellular Singlet Oxygen Production. The results of the *in vitro* single-line oxygen demonstrated that in a DMSO solution, the control group containing only DPBF experienced minimal change in absorbance at 414 nm when exposed to light. This indicated that the light had little impact on singlet oxygen production in the absence of photosensitizer VER. The absorption peaks in the solutions containing free VER, VER@HSA NPs, and APV@HSA NPs gradually decreased in intensity as the exposure time to light increased. This indicated that single-line oxygen was produced in the solution and decreased in the DPBF absorbance due to its consumption. The reduction in absorbance values at 414 nm in the DMSO solution for the free VER, the VER@HSA NPs, and the APV@HSA NPs were 55.91, 58.84, and 64.12%, respectively (as shown in Figure S2I–L). In aqueous solution, the values were 5.71, 6.21, and 10.83%, respectively (as shown in Figure S2M–P). The results of the single-linear oxygen assay demonstrated that the APV@HSA NP group had a higher single-linear oxygen generation capacity compared with the other groups, irrespective of the solvent used. These findings aligned closely with the fluorescence intensity results of free VER, VER@HSA NPs, and APV@HSA NPs in both DMSO and aqueous solutions, as detailed in the fluorescence absorption study. This experiment demonstrated that the photosensitizer VER, when integrated into this nanodelivery system, effectively generated singlet oxygen species upon light exposure. These results have significant implications for future PDT antitumor studies.

3.7. Cellular Uptake. The intracellular drug content plays a vital role in determining the effectiveness of the treatment. Moreover, research indicates that the internalization of nanoparticles enhances cellular uptake, thereby improving treatment efficacy.[49] Fluorescence microscopy and flow cytometry were employed to determine the uptake of the B16F10 cells. The findings revealed a significant time-dependent increase in the uptake of APV@HSA NPs. Concurrently, the fluorescence intensity of B16F10 cells treated with APV@HSA NPs and VER@HSA NPs was markedly higher than that of free VER at the corresponding time point (4 h), confirming the superior internalization efficiency of HSA. B16F10 cells secrete a surplus of cysteine-secreted proteins that function as albumin receptors, demonstrating high affinity and specificity for albumin. This

https://doi.org/10.1021/acsami.4c18469
ACS Appl. Mater. Interfaces XXXX, XXX, XXX−XXX

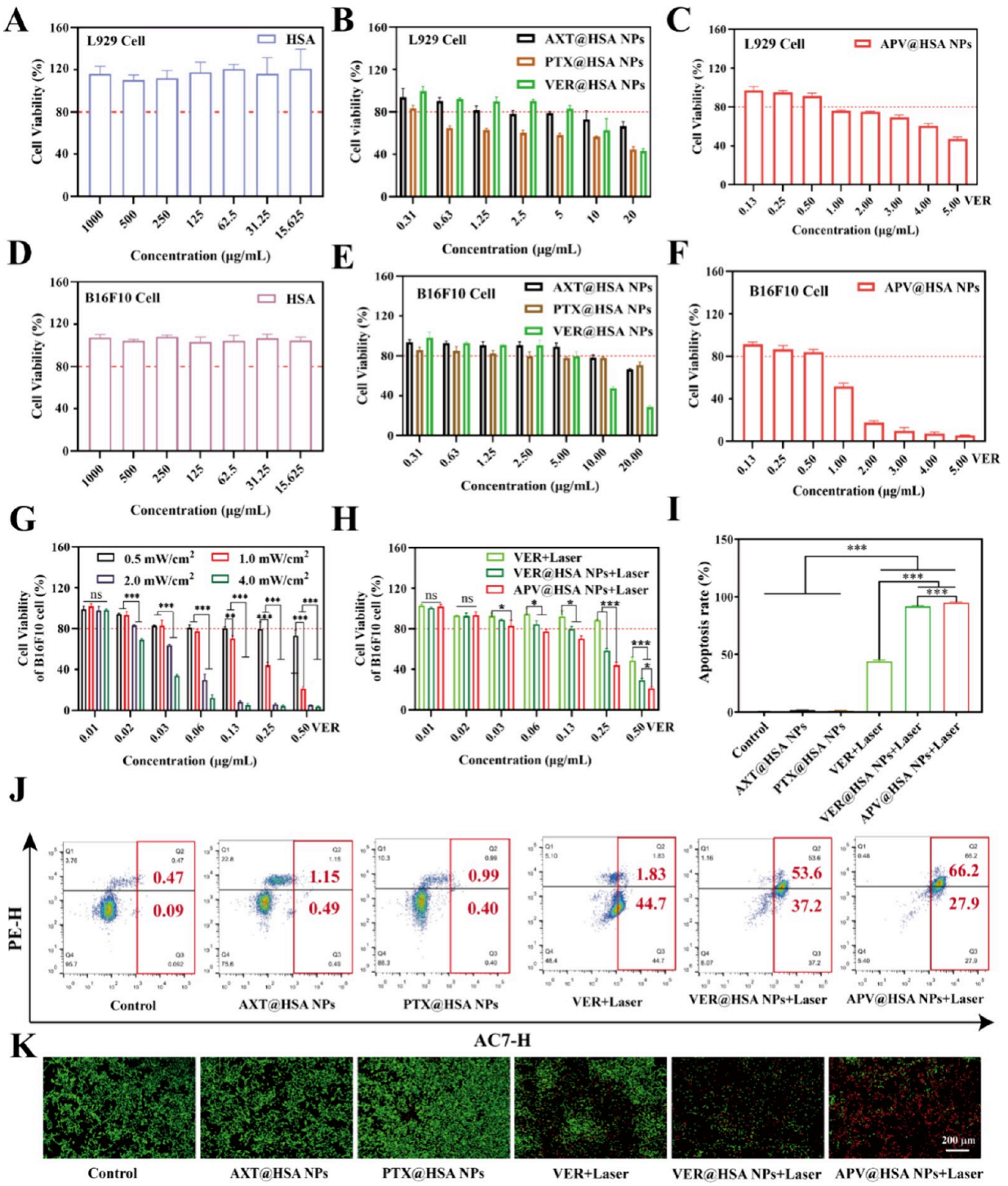

Figure 4. Cell cytotoxicity. (A) Examination of cytotoxicity of HSA on L929 cells. $n = 6$. (B, C) Examination of cytotoxicity of AXT@HSA NPs, PTX@HSA NPs, VER@HSA NPs, and APV@HSA NPs on L929 cells. $n = 6$. (D) Examination of cytotoxicity of HSA on B16F10 cells. $n = 6$. (E, F) Examination of cytotoxicity of AXT@HSA NPs, PTX@HSA NPs, VER@HSA NPs, and APV@HSA NPs on B16F10 cells. $n = 6$. (G) Phototoxicity of APV@HSA NPs to B16F10 cells at different laser power. $n = 6$. (H) Comparison of phototoxicity of free VER, VER@HSA NPs, and APV@HSA NPs to B16F10 cells (1 mW/cm^2, 10 min). $n = 6$. (I, J) Quantitative diagram and typical diagram of apoptotic results of B16F10 cells treated with different drugs. $n = 3$. (K) Staining results of live and dead cells after B16F10 cells were treated with various drugs. Scale bar: 200 μm. Values represented were means ± SD, $^*p < 0.05$, $^{**}p < 0.01$, $^{***}p < 0.001$.

characteristic aids in the transportation of albumin to tumor sites (as shown in Figure 3A–F).

3.8. APV@HSA NP *In Vitro* Cytological Evaluation. The cytotoxicity results of HSA on B16F10 cells and L929 cells showed good biocompatibility (>80% cell viability) to normal and melanoma cells even at a high concentration (1000 μg/mL), which is beneficial for its *in vivo* application (as shown in Figure 4A,D). The dark toxicity of AXT@HSA NPs, PTX@HSA NPs, VER@HSA NPs, and APV@HSA NPs on L929 cells and B16F10 cells was initially evaluated using an MTT

https://doi.org/10.1021/acsami.4c18469
ACS Appl. Mater. Interfaces XXXX, XXX, XXX−XXX

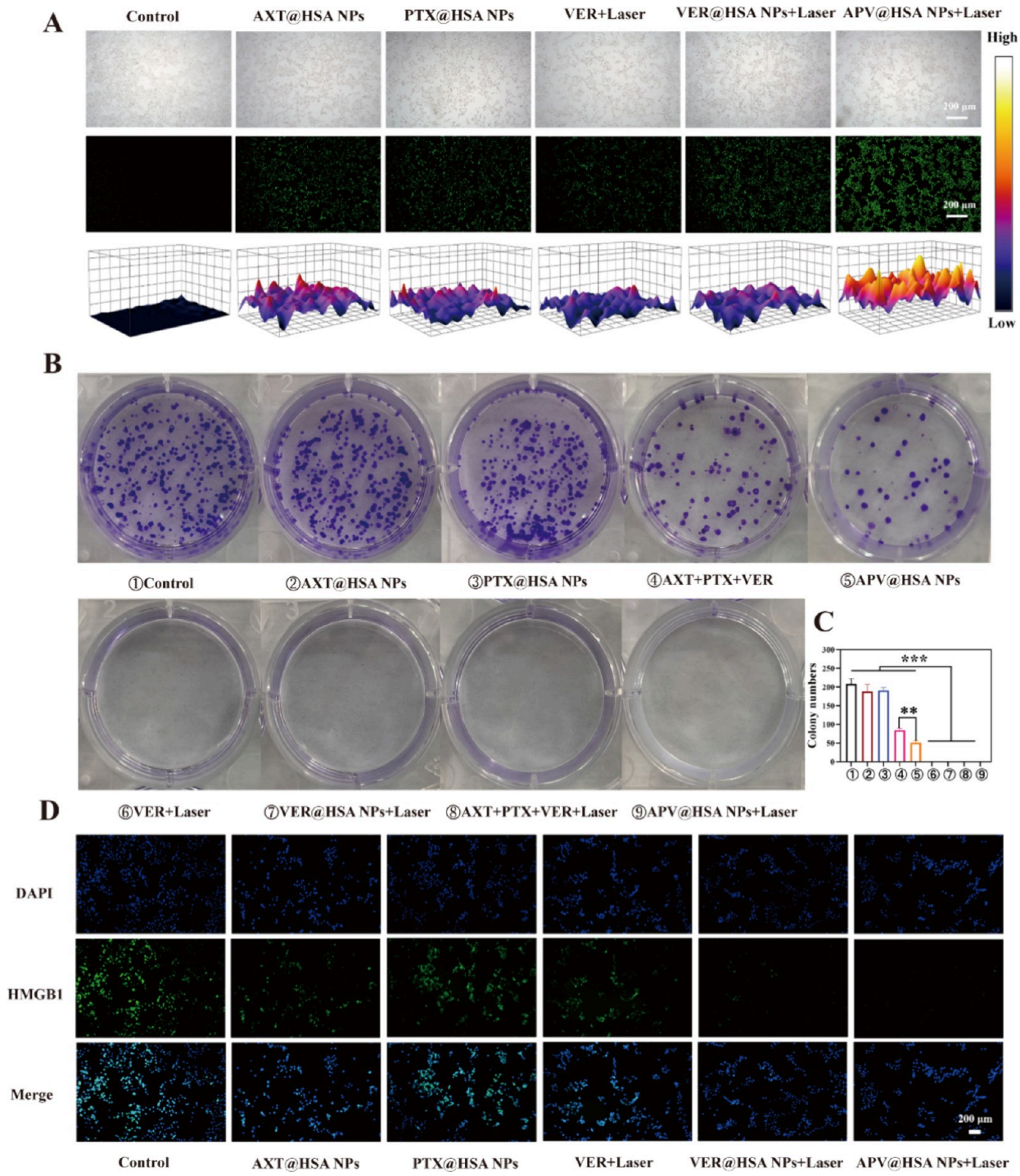

Figure 5. APV@HSA NPs *in vitro* cell assay of B16F10 cells. (A) ROS production in B16F10 cells treated with different drugs was observed by fluorescence microscopy and 3D surface plotting by ImageJ software (1 mW/cm^2, 10 min). Scale bar: 200 μm. (B, C) Typical and quantitative plots of cell colonies formed by B16F10 cells treated with different drugs (1 mW/cm^2, 10 min). n = 3. (D) Translocation of HMGB1 in B16F10 cells after treatment with different drugs was observed by fluorescence microscopy (1 mW/cm^2, 10 min). Scale bar: 200 μm. Values represented were means ± SD, *p < 0.05, **p < 0.01, ***p < 0.001.

assay. The findings demonstrated that the single-drug nanoparticles exhibited acceptable cellular viability at concentrations up to 5 μg/mL on B16F10 cells, while APV@HSA NPs demonstrated no notable dark toxicity up to 0.5 μg/mL on B16F10 cells. In comparison to B16F10 cells, APV@HSA NPs exhibited decreased cytotoxicity in L929 cells, indicating a higher efficacy in targeting tumor cells while ensuring greater safety for normal cells (as shown in Figure 4B,C,E,F). Consequently, this concentration was chosen for the following investigation of the formulation's phototoxicity, and any cytotoxicity observed within this range was attributed to PDT. Subsequently, phototoxicity of APV@HSA NPs (0.5 μg/mL) to B16F10 cells at different laser powers is as shown in Figure 4G. The cytotoxicity of APV@HSA NPs on B16F10 cells was notably higher than those of free VER and VER@HSA NPs (1 mW/cm^2, 10 min). This heightened cytotoxicity

https://doi.org/10.1021/acsami.4c18469
ACS Appl. Mater. Interfaces XXXX, XXX, XXX−XXX

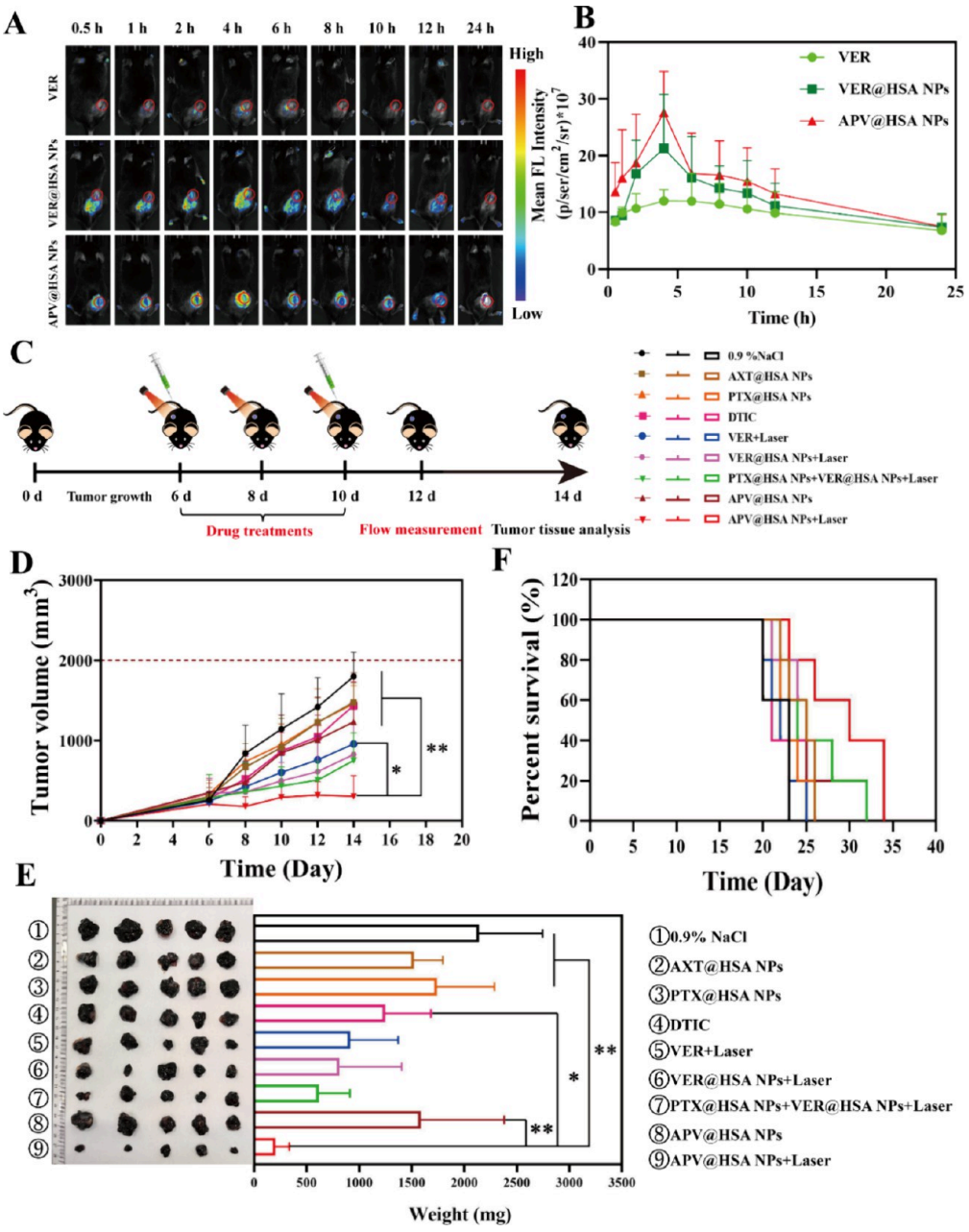

Figure 6. Biodistribution and *in vivo* antitumor efficacy. (A) Specific fluorescence imaging pictures and (B) quantitative analysis of tumor regions in mice 0.5−24 h after injection of free VER, VER@HSA NPs, and APV@HSA NPs. $n = 3$. (C) Schematic illustration of the establishment of a primary tumor model of melanoma and dosing regimen. (D) Tumor growth curves of mice in different treatment groups. $n = 5$. (E) Images and weight of tumor mass of each group after 14 days of administration. $n = 5$. (F) Survival curves of mice in different treatment groups. $n = 6$. Values represented were means ± SD, $*p < 0.05$, $**p < 0.01$, $***p < 0.001$.

can be attributed to the enhanced tumor-targeting capability of albumin nanoparticles and the synergistic effect of the triple drugs AXT, PTX, and VER (as shown in Figure 4H).

Subsequently, flow cytometry was utilized to identify apoptosis (Cyanine7-PI/Annexin V-APC), revealing that APV@HSA NPs exhibited notable antiproliferative and pro-apoptotic properties under laser exposure, suggesting promising antitumor effects *in vitro* (as shown in Figure 4I,J). Furthermore, the Calcein-AM/PI live−dead staining assay, conducted through the utilization of fluorescence microscopy, confirmed that APV@HSA NPs could induce a significant number of cell deaths under laser irradiation (as shown in Figure 4K). These results were consistent with the cytotoxicity and apoptosis evaluations.

3.9. Detection of Cell ROS Production. DCFH-DA, a ROS fluorescent probe, does not exhibit fluorescence itself. Rather, DCFH is generated intracellularly through deacetylation by esterase. DCF with green fluorescence is oxidized to form DCF in the presence of ROS. Consequently, the level of intracellular ROS production can be determined by detecting the strength of green fluorescence of DCF.[50] The control group exhibited minimal green fluorescence, while the AXT@HSA NP and PTX@HSA NP groups displayed a slight green fluorescence. Previous studies have indicated a connection between VEGF and ROS production[51] and highlighted the

https://doi.org/10.1021/acsami.4c18469
ACS Appl. Mater. Interfaces XXXX, XXX, XXX−XXX

capability of chemotherapeutic agents to stimulate ROS production in tumor cells.[52] During PDT treatment at 1 mW/cm^2 for 10 min, the APV@HSA NP group exhibited the highest fluorescence intensity, confirming its remarkable ability for cellular ROS generation. The 3D surface plotting, which assessed the fluorescence intensity based on the height and brightness of the model, yielded findings consistent with ROS analysis results obtained from fluorescence microscopy (as shown in Figure 5A).

3.10. Plate Cloning Test. The cell colony formation assay can assess the colony-forming ability of cells post-treatment with different drug groups. Consistent with the cytotoxicity assay, a specific number of colonies were detected in the control group, as well as in the AXT@HSA NP and PTX@HSA NP groups. It is noteworthy that the number of cellular colonies exhibited a decline in both the AXT+PTX+VER and APV@HSA NPs groups. The quantitative data indicated a statistically significant difference between the APV@HSA NP and AXT+PTX+VER groups, with the former displaying a lower colony count. These findings suggested that the nanoparticles of the albumin-loaded drug are more efficacious than the free drug treatment, which is likely attributable to the high internalization efficiency of the albumin carrier. In addition, no colony formation was observed in AXT+PTX +VER+Laser with the rest of the light groups, which also demonstrated the efficacy of PDT. The above experiments further confirmed the efficacy of APV@HSA NPs in inhibiting tumor cell proliferation (as shown in Figure 5B,C).

3.11. Determination of Biomarkers of Immunogenic Cell Death. Extracellularly released ATP plays as a "find me" signal by binding to dendritic cells and enhancing the infiltration of tumor monocytes.[53] The laser irradiation group exhibited a lower intracellular ATP content compared to those of the other groups. Particularly, the lowest intracellular ATP content was identified in the APV@HSA NP group, indicating a higher release of ATP extracellularly, leading to the most pronounced induction of ICD (as shown in Figure S3A).

During ICD in tumor cells, HMGB1 typically translocates from the nucleus of normal cells to the extracellular space. Extracellular HMGB1 can trigger toll-like receptors, promoting dendritic cell maturation.[54] The translocation of HMGB1 from the nucleus to the extracellular matrix was visualized by using fluorescence microscopy. The control group, AXT@HSA NP group, and PTX@HSA NP group exhibited a more pronounced green fluorescence. Interestingly, the laser irradiation group exhibited significantly reduced green fluorescence. Remarkably, the green fluorescence was minimal in the APV@HSA NP group, indicating substantial HMGB1 migration outside the cell (as shown in Figure 5D).

CRT emerges as a significant biomarker of ICD, playing as an "eat me" signal that induces antigen presentation dendritic cells to launch an immune response. Endoplasmic reticulum stress, instigated by intracellular ROS production, prompts the upregulation of CRT and its subsequent relocation to the surface of tumor cells.[55] Consequently, we detected CRT exposure on the surface of tumor cells via fluorescence microscopy. The levels of CRT were markedly increased in the laser irradiation group. Remarkably, the degree of CRT exposure correlated with the translocation of HMGB1 migration to the extracellular milieu, providing additional evidence that APV@HSA NPs substantially enhanced ICD and boosted the antitumor immune response (as shown in Figure S3B).

3.12. Biodistribution of APV@HSA NPs *In Vivo*. The promising antitumor effects and ability to stimulate immune responses observed *in vitro* prompted researchers to explore the *in vivo* antitumor effects of APV@HSA NPs. Initially, an *in vivo* imaging system was used to evaluate the tumor-targeting capacity of APV@HSA NPs in melanoma. The fluorescence signals in the tumor area of the free VER group showed a slight initial increase, followed by a gradual decrease. The fluorescence signals in the tumor area of the VER@HSA NP group and the APV@HSA NP group demonstrated a pattern of initial enhancement, followed by a decrease, reaching a peak at the fourth hour (as shown in Figure 6A,B). The tumors in the APV@HSA NP group displayed more intense fluorescence signals compared with those in the free VER group. The accumulation of nanodrugs in tumor regions may be attributed to the interaction of albumin with its binding receptors, such as gp60 (or SPARC) and the EPR effect, which facilitates the targeted accumulation of the albumin nanodrug delivery system in tumor tissues. Additionally, light exposure was initiated at the fourth hour after the administration of the drug with the aim of maximizing the PDT effect *in vivo*.

3.13. *In Vivo* Evaluation of Antitumor Efficacy and Safety. Considering the promising *in vitro* results showcasing the capability of HSA nanomedicines to induce an ICD effect and accumulate in tumors, our study aimed to evaluate their *in vivo* antitumor efficacy, antitumor immune response, and *in vivo* safety in primary tumor models. The various formulations were administered on days 6, 8, and 10 via the intravenous route following a straightforward dosing regimen, as illustrated in the schematic diagram (as shown in Figure 6C). Throughout the treatment period, the body weights of mice in all groups exhibited an increasing trend during the treatment period, indicating that nanomedicine did not impact the appetite of mice (as shown in Figure S5A). Tumor volume was assessed at 2-day intervals. Mice treated with 0.9%NaCl showed enhanced tumor growth. In contrast, the AXT@HSA NP, PTX@HSA NP, DTIC, and APV@HSA NP groups exhibited slight tumor regression. The laser irradiation groups displayed a notable decrease in tumor volume with the APV@HSA NPs+Laser group showing the most significant inhibition of primary tumor growth. The tumor volume was larger in the PTX@HSA NPs+VER@HSA NPs+Laser group compared to that in the APV@HSA NPs+Laser group. This observation validates the efficacy of incorporating the antiangiogenic drug AXT, which effectively suppresses the primary tumor volume. These results support the synergistic approach of chemical-photodynamic-immune treatment of melanoma (as shown in Figure 6D and Figure S4A). Furthermore, the trends in tumor weight and tumor growth inhibition were similar among the various treatment groups, showing the most significant tumor suppression in the APV@HSA NPs+Laser group (as shown in Figure 6E and Figure S5B). The tumor burdens in all treatment groups were less than 10%, meeting the animal welfare end points (as shown in Figure S5C). Concurrently, the results of the mouse survival assay demonstrated that all administration groups could increase the median survival of mice, with the APV@HSA NP group showing the most significant enhancement (Figure 6F). H&E staining is a commonly used technique for identifying apoptosis and tissues damage in tumor samples. The APV@HSA NPs+Laser group exhibited significant cytoplasmic damage, nuclear atrophy, and extensive tissue damage compared to the other groups. Afterward, TUNEL staining and Ki67 histochemistry were

https://doi.org/10.1021/acsami.4c18469
ACS Appl. Mater. Interfaces XXXX, XXX, XXX−XXX

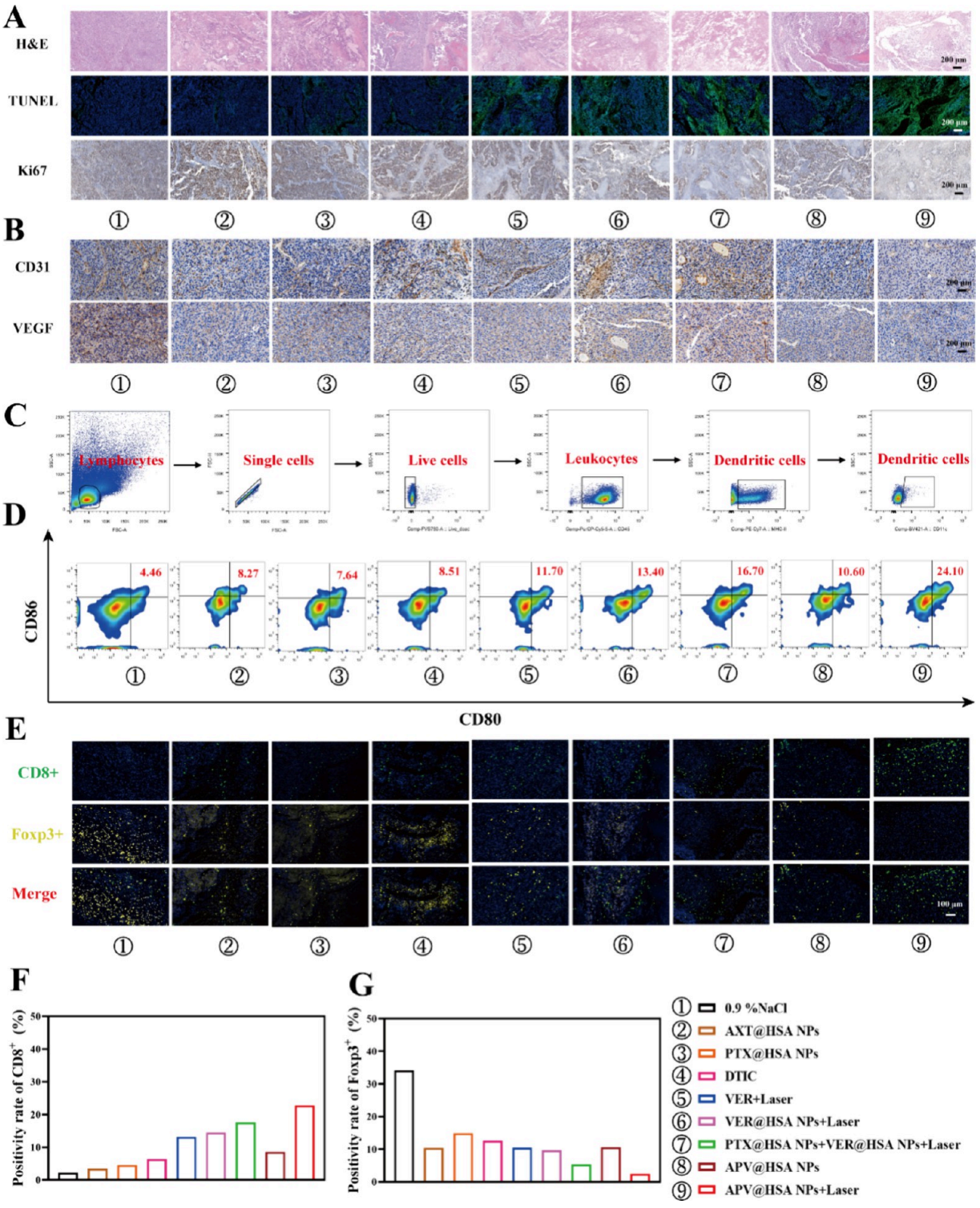

Figure 7. *In vivo* safety and immunological reaction of APV@HSA NPs in the situ tumor model. (A) H&E, TUNEL, and Ki67 staining images of tumors after different administration treatments. Scale bar: 200 μm. (B) CD31 and VEGF staining images of tumors after different administration treatments. Scale bar: 200 μm. (C) Gating strategies for flow cytometry analysis of DCs cells in lymph nodes. (D) Typical plot of the percentage of DCs cells in lymph nodes of different dosing groups. (E) Immunofluorescence images of recruited $CD8^+$ T and $Foxp3^+$ cells in the in situ tumor section. Scale bar: 100 μm. (F, G) Positivity of $CD8^+$ T and $Foxp3^+$ cells. Values represented were means ± SD, $*p$ <0.05, $**p$ <0.01, $***p$ <0.001.

utilized to confirm the induction of apoptosis and inhibition of proliferation effects. Minimal differences were observed in the TUNEL staining and Ki67 immunohistochemistry results among the AXT@HSA NP, PTX@HSA NP, DTIC, and APV@HSA NP groups compared with the 0.9%NaCl group. The group subjected to the laser irradiation group displayed a higher count of green fluorescent signals and a lower count of brown punctate signals. Particularly noteworthy was the APV@HSA NPs+Laser group, which showed the largest areas of green fluorescence and the lowest number of brown

https://doi.org/10.1021/acsami.4c18469
ACS Appl. Mater. Interfaces XXXX, XXX, XXX−XXX

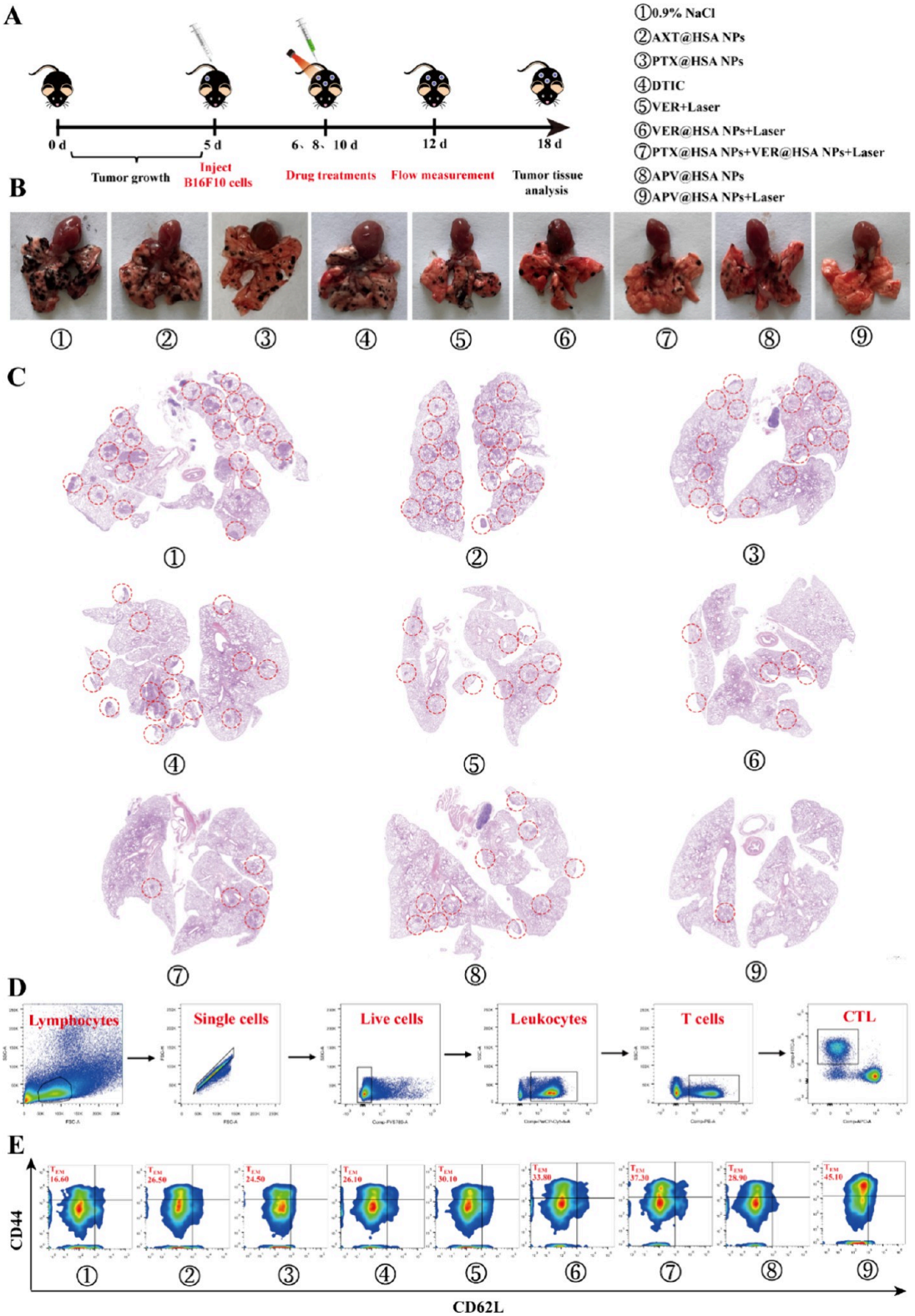

Figure 8. Study of *in vivo* antimetastatic. (A) Schematic diagram of the dosing regimen for inhibition of melanoma lung metastasis. (B) Typical images of lung metastatic nodules in the B16F10 melanoma model. (C) H&E staining diagram of mouse lung tissue. Scale bar: 1000 μm. (D) Flow cytometry analysis of gating strategies for splenic effector memory T cells. (E) Typical plot of the percentage of effector memory T cells in the spleen of different dosing groups. Values represented were means ± SD, *p <0.05, **p <0.01, ***p <0.001.

spots. These findings suggested that the APV@HSA NPs +Laser group induced a significant number of apoptotic events and effectively restrained tumor proliferation in mouse tumor cells, demonstrating remarkable antitumor efficacy (as shown in Figure 7A). The results demonstrate that APV@HSA NPs can effectively induce synergy through chemo-photodynamic-immune mechanisms, effectively targeting and eliminating melanoma cells. For the assessment of *in vivo* safety, cardiac,

https://doi.org/10.1021/acsami.4c18469
ACS Appl. Mater. Interfaces XXXX, XXX, XXX−XXX

hepatic, and renal functions were further evaluated by measuring serum levels of ALT, BUN, CRE, and CK. Compared with the 0.9%NaCl group, no significant differences were observed in ALT, BUN, CK, and CRE levels across the drug treatment groups, with all blood biochemical parameters staying within the expected normal range (as shown in Figure S5D−G). Histological examination of major organs in mice across all groups revealed no notable pathological damage or morphological changes, including those of the heart, liver, spleen, lungs, and kidneys. Administering the drug at multiple doses at the pathological level demonstrated the lack of substantial toxic effects on major organs, thus reinforcing the nanoparticles' favorable *in vivo* biosafety profile (as shown in Figure S5H).

3.14. Synergistic Immune Responses. Building upon the promising initial results in combating primary melanoma tumors, we subsequently delved into scrutinizing the potential mechanism involving chemo-photodynamic mediation of the antitumor immune response *in vivo*. Throughout tumor advancement, the hypoxic microenvironment promotes the secretion of cytokines, chemokines, and growth factors, notably, VEGF. These molecules interact with peripheral endothelial cells to stimulate tumor angiogenesis. Prolonged elevation of VEGF can lead to the development of abnormal and permeable neovessels, aiding in tumor cell infiltration and metastasis. Furthermore, studies have shown that VEGF not only promotes the proliferation of immunosuppressive cells such as TAMs and Tregs but also hinders the maturation of dendritic cells and the functionality of T lymphocytes, leading to less effective immune responses. CD31, a crucial marker of VEGF, demonstrates normalization closely correlated with the downregulation of CD31 expression.[56] Axitinib, a VEGFR inhibitor exhibiting high affinity at the nanoscale, normalizes the vasculature and effectively suppresses the expression and secretion of VEGF-mediated angiogenic factors.[57] The histological analysis of CD31 and VEGF showed a decrease in brown punctate signals in the axitinib-containing group compared to the 0.9%NaCl group, with notably lower VEGF levels in the APV@HSA NPs+Laser group (as shown in Figure 7B). Lower VEGF levels facilitate normalization of the vascular system, potentially ameliorating the hypoxic tumor environment. This indirect effect enhances the effectiveness of chemotherapy and PDT, intensifying the induced ICD with combined chemo-PDT, thereby improving immunotherapy. Remarkably, the decrease in VEGF levels not only suppressed the proliferation of immunosuppressive cells but also bolstered the immune response. Subsequently, antigen-presenting cells known as DCs were quantified using flow cytometry to evaluate the activation level of the body's immune system response. The double-positive cell clusters of MHC-II and CD11c, characteristics of DCs, were identified and isolated for detailed examination through a gating technique. Subsequently, the double-positive cell clusters of CD80 and CD86, markers of mature DCs, were also isolated for analysis (as shown in Figure 7C). The APV@HSA NPs+Laser group exhibited a substantial increase in the proportion of mature DCs, reaching 24.10%, which was 4.4-fold higher than that observed in the 0.9%NaCl group (4.46%). This finding implied the activation of the immune system (as shown in Figure 7D). Flow cytometry results validated that the combined chemo-photodynamic-immunotherapy strategy facilitated the generation of mature lymphocytes (as shown in Figure S5I). Notably, the infiltration of cytotoxic T lymphocytes ($CD8^+$ T) in the tumor region serves as a crucial indicator of antitumor immunity. Compared with the 0.9%NaCl group and the nonlight-irradiated group, the laser-irradiated group showed increased green fluorescence signal ($CD8^+$ T). Notably, the APV@HSA NPs+Laser group exhibited the greatest density of green fluorescence signal, signifying substantial infiltration of $CD8^+$ T lymphocytes into the tumor tissue. Conversely, the expression of immunosuppressive cells $Foxp3^+$ (yellow fluorescence) was higher in the 0.9%NaCl group than in the nonlight-irradiated group. Conversely, a notable decrease in $Foxp3^+$ expression was evident in the laser irradiation group. As expected, the lowest expression of $Foxp3^+$ was observed in the APV@HSA NPs+Laser group, indicating a significant enhancement in the immunosuppressive microenvironment (as shown in Figure 7E). Quantitative results of $CD8^+$ and $Foxp3^+$ positivity were consistent with immunofluorescence results (as shown in Figure 7F,G). In conclusion, the APV@HSA NPs+Laser group demonstrated the ability to not only directly eliminate melanoma cells but also promote the maturation of dendritic cells and the activation of cytotoxic T lymphocytes, thereby displaying strong antitumor immune efficacy. Initial findings indicated that the designed HSA drug delivery system may enhance the body's antitumor immune response.

3.15. *In Vivo* Evaluation of Antilung Metastases. Melanoma is a highly aggressive and rapidly metastasizing cancer, leading to significant patient mortality and contributing substantially to low survival rates.[58] A successful tumor immunotherapy should be able to induce an immune response that extends beyond the confines of the primary tumor tissue. Following the encouraging results witnessed in the primary melanoma, our study advanced to assess the antipulmonary metastatic properties of APV@HSA NPs. This was accomplished through the intravenous administration of B16F10 cells in mice (as shown in Figure 8A). Upon completion of the treatment period, the lung organs of the mice in each experimental group were excised. Clearly visible black tumor nodules were observed in the 0.9%NaCl group, while the other groups exhibited a notable decrease in tumor nodule formation. Quantitative analysis of lung tissue confirmed these observations. The group treated with APV@HSA NPs +Laser exhibited the fewest tumor nodules and the healthiest lung tissues. This outcome may be attributed to the synergistic antitumor effects of PTX as a chemotherapy agent, VER as a photosensitizer, and axitinib as a VEGF inhibitor. Additionally, the reversal of the tumor's immune-suppressive microenvironment and the stimulation of systemic antitumor immune responses likely contributed to this outcome (as shown in Figure 8B and Figure S6A). Furthermore, H&E staining of the lungs revealed similar results, demonstrating a notable decrease in the quantity of lung tumor nodules in the APV@HSA NPs +Laser group (as shown in Figure 8C). It is reasonable to infer that the APV@HSA NP chemo-photodynamic-immunotherapy nanoplatform shows promise in inhibiting tumor metastasis. Additionally, effector T cells have the ability to produce cytokines, which are crucial in the establishment of long-term immune memory against the tumors. The capacity to generate long-term immune responses is a key feature of the immune system. Based on these findings, the percent of T_{EM} in spleens was determined to explore the ability of APV@HSA NPs to stimulate immune memory. T_{EM} characterized by CD62L-negative and CD44-positive cell clusters were identified through a gating strategy (as shown in Figure 8D). Compared

https://doi.org/10.1021/acsami.4c18469
ACS Appl. Mater. Interfaces XXXX, XXX, XXX−XXX

with the 0.9%NaCl group (17.13 ± 0.51%), the percentage of T_{EM} in the APV@HSA NPs+Laser group was significantly elevated to (42.03 ± 3.05%). These results indicated that the chemo-photodynamic-immunological synergistic effect of the nanomedicine enhanced immune memory in the host (as shown in Figure 8E and Figure S6B). These findings reaffirmed the enhanced potential of the amplified APV@HSA NPs in mediating immune responses to prevent tumor metastasis.

4. CONCLUSIONS

In conclusion, a rationally designed HSA nanopharmaceutical delivery system (APV@HSA NPs) has been formulated with the aim of effectively eradicating melanoma cells. The design of this system is geared toward boosting the effectiveness of chemo-photodynamic-immunotherapy through a "three-pronged" approach. The designed APV@HSA NPs augment tumor accumulation through the overexpression of albumin-binding proteins within tumors. The localized delivery of PTX and VER at the tumor site demonstrated that the integrated chemo-PDT concurrently and synergistically elicited DAMPs within tumor cells, subsequently recognized by DCs. Moreover, the release of AXT inhibited VEGFR activity, while facilitating immune cell infiltration. Thus, our engineered APV@HSA NPs exhibited enhanced chemo-photodynamic immunotherapy by modulating the tumor microenvironment, potentially offering promising avenues for combination therapies that activate the host immune system against primary tumor progression and metastasis. These findings not only provide valuable insights but also serve as practical demonstrations that could guide further research in the realm of melanoma treatment.

■ ASSOCIATED CONTENT

Data Availability Statement

Data will be made available on request.

Supporting Information

The Supporting Information is available free of charge at https://pubs.acs.org/doi/10.1021/acsami.4c18469.

Detailed experimental procedures; dark toxicity of AXT, PTX, and VER in B16F10 cells; phototoxicity of VER in B16F10 cells; TEM and zeta potential diagram of AXT@HSA NPs, PTX@HSA NPs, VER@HSA NPs, and APV@HSA NPs; ultraviolet−visible absorption spectra of AXT@HSA NPs, PTX@HSA NPs, and VER@HSA NPs; fluorescence spectra of AXT, PTX, VER, and their albumin nanomaterials, as well as APV@HSA NPs in DMSO solution; VER, VER@HSA NP, and APV@HSA NP fluorescence imaging results in DMSO and aqueous solutions; infrared spectrum of APV@HSA NPs; X-ray diffraction of APV@HSA NPs; differential scanning calorimetry of APV@HSA NPs; APV@HSA NP stability evaluation of NP solution; evaluation of laser irradiation stability of different preparations; appearance of APV@HSA NPs in different lyophilized protectants and pictures after redissolving; hemolysis plots for different concentrations of APV@HSA NP solutions; absorbance of different preparations of DMSO solution at 414 nm varies with the illumination time; absorbance of different preparations of aqueous solution at 414 nm varies with the illumination time; evaluation of the resolubility of APV@HSA NPs after lyophilization; exposure of CRT in B16F10 cells after treatment with different drugs observed by a fluorescence microscope; typical pictures of mice at days 6, 10, and 14 in different administration groups; changes of body weight of mice in different administration groups during treatment; tumor control rate in different administration groups; relative tumor burden in different administration groups; evaluation of blood biochemical indexes of mice in each group after drug treatment; results of H&E staining of organs in each group after drug treatment; proportion of DC cells in lymph nodes of mice in each group after drug treatment; number of tumor nodules in lung tissue of mice in each group after drug treatment; and proportion of T_{EM} in spleen of mice in each group after drug treatment (PDF)

■ AUTHOR INFORMATION

Corresponding Authors

Hongtao Song − *Department of Pharmacy, The 900th Hospital of Joint Logistic Support Force, PLA, Fuzhou 350025, China*; Email: sohoto@vip.163.com

Xin Zhou − *Department of Pharmacy, The 900th Hospital of Joint Logistic Support Force, PLA, Fuzhou 350025, China*; Email: libaihuamao@yahoo.com.cn

Zhihong Liu − *Department of Pharmacy, The 900th Hospital of Joint Logistic Support Force, PLA, Fuzhou 350025, China*; orcid.org/0009-0009-9560-3368; Email: liuzh827@sina.cn

Authors

Fei Wu − *Department of Pharmacy, The 900th Hospital of Joint Logistic Support Force, PLA, Fuzhou 350025, China*

Xianquan Feng − *Fujian Provincial Key Laboratory of Transplant Biology, Laboratory of Basic Medicine, The 900th Hospital of Joint Logistic Support Force, PLA, Fuzhou 350025, China*

Wenhao Gao − *Department of Pharmacy, The 900th Hospital of Joint Logistic Support Force, PLA, Fuzhou 350025, China*

Lingjun Zeng − *Department of Pharmacy, The 900th Hospital of Joint Logistic Support Force, PLA, Fuzhou 350025, China*; orcid.org/0009-0001-7517-4991

Bingbing Xu − *Department of Pharmacy, The 900th Hospital of Joint Logistic Support Force, PLA, Fuzhou 350025, China*

Zhenzhen Chen − *Department of Clinical Pharmacy, The 900th Hospital of Joint Logistic Support Force, PLA, Fuzhou, Fujian Province 350025, China*

Changqing Zheng − *Department of Pharmacy, The 900th Hospital of Joint Logistic Support Force, PLA, Fuzhou 350025, China*

Xiaomu Hu − *Department of Pharmacy, The 900th Hospital of Joint Logistic Support Force, PLA, Fuzhou 350025, China*

Shiying Xu − *Department of Pharmacy, The 900th Hospital of Joint Logistic Support Force, PLA, Fuzhou 350025, China*

Complete contact information is available at: https://pubs.acs.org/10.1021/acsami.4c18469

Author Contributions

F.W. and X.F. contributed equally to this article and contributed to the conception, design, writing of the original draft, and the experiment of nanoparticle synthesis study. W.G. conducted methodology, formal analysis, and data management for the article. L.Z. managed and investigated the article data. B.X. investigated the article data. Z.C. investigated the

https://doi.org/10.1021/acsami.4c18469
ACS Appl. Mater. Interfaces XXXX, XXX, XXX−XXX

article data. C.Z. investigated the article data. X.H. investigated the article data. S.X. investigated the article data.

Funding

This work was supported by the Natural Science Foundation of Fujian Province [grant numbers: 2022J0064, 2024J08094, and 2022J011092].

Notes

The authors declare no competing financial interest.

■ ACKNOWLEDGMENTS

We appreciate the Public Technology Service Center of Fujian Medical University for technical assistance and Phadcalc (www.phadcalc.com) for the molecular docking simulation.

■ REFERENCES

(1) Fernandez-Flores, A. Modern Concepts in Melanocytic Tumors. *Actas dermo-sifiliograficas* **2023**, *114*, 402−412.
(2) Long, G. V.; Swetter, S. M.; Menzies, A. M.; Gershenwald, J. E.; Scolyer, R. A. Cutaneous melanoma. *Lancet (London, England)* **2023**, *402*, 485−502.
(3) Slominski, A.; Wortsman, J.; Carlson, A. J.; Matsuoka, L. Y.; Balch, C. M.; Mihm, M. C. Malignant melanoma. *Archives of pathology & laboratory medicine* **2001**, *125*, 1295−1306.
(4) Saaiq, M.; Zalaudek, I.; Rao, B.; Lee, Y.; Rudnicka, L.; Czuwara, J.; Giuffrida, R.; Wollina, U.; Jafferany, M.; Lotti, T.; Grabbe, S.; Goldust, M. A brief synopsis on scalp melanoma. *Dermatol. Ther.* **2020**, *33*, No. e13795.
(5) Markovic, S. N.; Erickson, L. A.; Flotte, T. J.; Kottschade, L. A.; McWilliams, R. R.; Jakub, J. W.; Farley, D. R.; Tran, N. V.; Schild, S. E.; Olivier, K. R.; Vuk-Pavlovic, S.; Sekulic, A.; Weenig, R. H.; Pulido, J. S.; Quevedo, J. F.; Vile, R. G.; Wiseman, G. A.; Stoian, I.; Pittelkow, M. R.; Melanoma Study Group of the Mayo Clinic Cancer Center. Metastatic malignant melanoma. *G. Ital. Dermatol. Venereol.* **2009**, *144*, 1−26.
(6) Lee, K. A.; Nathan, P. Cutaneous Melanoma - A Review of Systemic Therapies. *Acta dermato-venereologica* **2020**, *100*, adv00141.
(7) Schreiber, R. D.; Old, L. J.; Smyth, M. J. Cancer immunoediting: integrating immunity's roles in cancer suppression and promotion. *Science (New York, N.Y.)* **2011**, *331*, 1565−1570.
(8) Marzagalli, M.; Ebelt, N. D.; Manuel, E. R. Unraveling the crosstalk between melanoma and immune cells in the tumor microenvironment. *Seminars in cancer biology* **2019**, *59*, 236−250.
(9) Keenan, T. E.; Tolaney, S. M. Role of Immunotherapy in Triple-Negative Breast Cancer. *Journal of the National Comprehensive Cancer Network: JNCCN* **2020**, *18*, 479−489.
(10) Sweeney, E. E.; Cano-Mejia, J.; Fernandes, R. Photothermal Therapy Generates a Thermal Window of Immunogenic Cell Death in Neuroblastoma. *Small* **2018**, *14*, No. e1800678.
(11) Tesniere, A.; Panaretakis, T.; Kepp, O.; Apetoh, L.; Ghiringhelli, F.; Zitvogel, L.; Kroemer, G. Molecular characteristics of immunogenic cancer cell death. *Cell death and differentiation* **2008**, *15*, 3−12.
(12) Pelka, S.; Guha, C. Enhancing Immunogenicity in Metastatic Melanoma: Adjuvant Therapies to Promote the Anti-Tumor Immune Response. *Biomedicines* **2023**, *11*, 2245.
(13) Zheng, P.; Ding, B.; Jiang, Z.; Xu, W.; Li, G.; Ding, J.; Chen, X. Ultrasound-Augmented Mitochondrial Calcium Ion Overload by Calcium Nanomodulator to Induce Immunogenic Cell Death. *Nano Lett.* **2021**, *21*, 2088−2093.
(14) Zhai, J.; Gu, X.; Liu, Y.; Hu, Y.; Jiang, Y.; Zhang, Z. Chemotherapeutic and targeted drugs-induced immunogenic cell death in cancer models and antitumor therapy: An update review. *Front. Pharmacol.* **2023**, *14*, No. 1152934.
(15) Qiu, X.; Qu, Y.; Guo, B.; Zheng, H.; Meng, F.; Zhong, Z. Micellar paclitaxel boosts ICD and chemo-immunotherapy of metastatic triple negative breast cancer. *Journal of controlled release: official journal of the Controlled Release Society* **2022**, *341*, 498−510.
(16) Wanderley, C. W.; Colón, D. F.; Luiz, J. P. M.; Oliveira, F. F.; Viacava, P. R.; Leite, C. A.; Pereira, J. A.; Silva, C. M.; Silva, C. R.; Silva, R. L.; Speck-Hernandez, C. A.; Mota, J. M.; Alves-Filho, J. C.; Lima-Junior, R. C.; Cunha, T. M.; Cunha, F. Q. Paclitaxel Reduces Tumor Growth by Reprogramming Tumor-Associated Macrophages to an M1 Profile in a TLR4-Dependent Manner. *Cancer research* **2018**, *78*, 5891−5900.
(17) Yang, C. H.; Horwitz, S. B. Taxol(®): The First Microtubule Stabilizing Agent. *International journal of molecular sciences* **2017**, *18*, 1733.
(18) Meng, F.; Wang, J.; He, Y.; Cresswell, G. M.; Lanman, N. A.; Lyle, L. T.; Ratliff, T. L.; Yeo, Y. A single local delivery of paclitaxel and nucleic acids via an immunoactive polymer eliminates tumors and induces antitumor immunity. *Proc. Natl. Acad. Sci. U.S.A.* **2022**, *119*, No. e2122595119.
(19) Xi, Y.; Chen, L.; Tang, J.; Yu, B.; Shen, W.; Niu, X. Amplifying "eat me signal" by immunogenic cell death for potentiating cancer immunotherapy. *Immunological reviews* **2024**, *321*, 94−114.
(20) Liu, S.; Kong, X.; Fang, Y.; He, Z.; Wu, H.; Ji, J.; Yang, X.; Ye, L.; Zhai, G. A dual-sensitive nanoparticle-mediated deepening synergistic therapy strategy involving DNA damage and ICD stimuli to treat triple-negative breast cancer. *Biomaterials science* **2023**, *11*, 6325−6341.
(21) Ren, G.; Li, Y.; Ping, C.; Duan, D.; Li, N.; Tang, J.; Wang, R.; Guo, W.; Niu, X.; Ji, Q.; Zhang, G.; Wang, R.; Zhang, S. Docetaxel prodrug and hematoporphyrin co-assembled nanoparticles for anti-tumor combination of chemotherapy and photodynamic therapy. *Drug delivery* **2022**, *29*, 3358−3369.
(22) Wang, C.; Zhang, R.; He, J.; Yu, L.; Li, X.; Zhang, J.; Li, S.; Zhang, C.; Kagan, J. C.; Karp, J. M.; Kuai, R. Ultrasound-responsive low-dose doxorubicin liposomes trigger mitochondrial DNA release and activate cGAS-STING-mediated antitumour immunity. *Nat. Commun.* **2023**, *14*, 3877.
(23) Chen, Z.; Sun, Y.; Wang, J.; Zhou, X.; Kong, X.; Meng, J.; Zhang, X. Dual-Responsive Triple-Synergistic Fe-MOF for Tumor Theranostics. *ACS Nano* **2023**, *17*, 9003−9013.
(24) Mkhobongo, B.; Chandran, R.; Abrahamse, H. The Role of Melanoma Cell-Derived Exosomes (MTEX) and Photodynamic Therapy (PDT) within a Tumor Microenvironment. *International journal of molecular sciences* **2021**, *22*, 9726.
(25) Castano, A. P.; Mroz, P.; Hamblin, M. R. Photodynamic therapy and anti-tumour immunity. *Nature reviews. Cancer* **2006**, *6*, 535−545.
(26) Duan, X.; Chan, C.; Lin, W. Nanoparticle-Mediated Immunogenic Cell Death Enables and Potentiates Cancer Immunotherapy. *Angewandte Chemie (International ed. in English)* **2019**, *58*, 670−680.
(27) Ji, B.; Wei, M.; Yang, B. Recent advances in nanomedicines for photodynamic therapy (PDT)-driven cancer immunotherapy. *Theranostics* **2022**, *12*, 434−458.
(28) Phua, S. Z. F.; Yang, G.; Lim, W. Q.; Verma, A.; Chen, H.; Thanabalu, T.; Zhao, Y. Catalase-Integrated Hyaluronic Acid as Nanocarriers for Enhanced Photodynamic Therapy in Solid Tumor. *ACS Nano* **2019**, *13*, 4742−4751.
(29) Dolmans, D. E.; Fukumura, D.; Jain, R. K. Photodynamic therapy for cancer. *Nature reviews. Cancer* **2003**, *3*, 380−387.
(30) Fan, J. X.; Liu, M. D.; Li, C. X.; Hong, S.; Zheng, D. W.; Liu, X. H.; Chen, S.; Cheng, H.; Zhang, X. Z. A metal-semiconductor nanocomposite as an efficient oxygen-independent photosensitizer for photodynamic tumor therapy. *Nanoscale horizons* **2017**, *2*, 349−355.
(31) Agostinis, P.; Berg, K.; Cengel, K. A.; Foster, T. H.; Girotti, A. W.; Gollnick, S. O.; Hahn, S. M.; Hamblin, M. R.; Juzeniene, A.; Kessel, D.; Korbelik, M.; Moan, J.; Mroz, P.; Nowis, D.; Piette, J.; Wilson, B. C.; Golab, J. Photodynamic therapy of cancer: an update. *CA: a cancer journal for clinicians* **2011**, *61*, 250−281.
(32) Fan, F.; Schimming, A.; Jaeger, D.; Podar, K. Targeting the tumor microenvironment: focus on angiogenesis. *J. Oncol.* **2012**, *2012*, No. 281261.

https://doi.org/10.1021/acsami.4c18469
ACS Appl. Mater. Interfaces XXXX, XXX, XXX−XXX

(33) Jain, R. K. Normalization of tumor vasculature: an emerging concept in antiangiogenic therapy. *Science (New York, N.Y.)* **2005**, *307*, 58−62.
(34) Zhou, Y.; Ren, X.; Hou, Z.; Wang, N.; Jiang, Y.; Luan, Y. Engineering a photosensitizer nanoplatform for amplified photodynamic immunotherapy via tumor microenvironment modulation. *Nanoscale horizons* **2021**, *6*, 120−131.
(35) Fukumura, D.; Kloepper, J.; Amoozgar, Z.; Duda, D. G.; Jain, R. K. Enhancing cancer immunotherapy using antiangiogenics: opportunities and challenges. *Nature reviews. Clinical oncology* **2018**, *15*, 325−340.
(36) Jain, R. K. Normalizing tumor microenvironment to treat cancer: bench to bedside to biomarkers. *Journal of clinical oncology: official journal of the American Society of Clinical Oncology* **2013**, *31*, 2205−2218.
(37) Facciabene, A.; Peng, X.; Hagemann, I. S.; Balint, K.; Barchetti, A.; Wang, L. P.; Gimotty, P. A.; Gilks, C. B.; Lal, P.; Zhang, L.; Coukos, G. Tumour hypoxia promotes tolerance and angiogenesis via CCL28 and T(reg) cells. *Nature* **2011**, *475*, 226−230.
(38) Läubli, H.; Müller, P.; D'Amico, L.; Buchi, M.; Kashyap, A. S.; Zippelius, A. The multi-receptor inhibitor axitinib reverses tumor-induced immunosuppression and potentiates treatment with immune-modulatory antibodies in preclinical murine models. *Cancer immunology, immunotherapy: CII* **2018**, *67*, 815−824.
(39) Bergers, G.; Benjamin, L. E. Tumorigenesis and the angiogenic switch. *Nature reviews. Cancer* **2003**, *3*, 401−410.
(40) Ji, T.; Feng, B.; Shen, J.; Zhang, M.; Hu, Y.; Jiang, A.; Zhu, D.; Chen, Y.; Ji, W.; Zhang, Z.; Zhang, H.; Li, F. An Avascular Niche Created by Axitinib-Loaded PCL/Collagen Nanofibrous Membrane Stabilized Subcutaneous Chondrogenesis of Mesenchymal Stromal Cells. *Adv. Sci.* **2021**, *8*, No. e2100351.
(41) Ji, M.; Liu, H.; Liang, X.; Wei, M.; Shi, D.; Gou, J.; Yin, T.; He, H.; Tang, X.; Zhang, Y. Tumor cells are under siege from all sides: Tumor Cell-Mimic Metal−Org anic framework nanoparticles triggering Cuproptosis/Ferroptosis/Apopto sis for Chemo-Chemodynamic-Photothermal-Immunological synergistic anti tumor therapy. *Chem. Eng. J.* **2024**, *485*, No. 149640.
(42) Peng, C. L.; Lin, H. C.; Chiang, W. L.; Shih, Y. H.; Chiang, P. F.; Luo, T. Y.; Cheng, C. C.; Shieh, M. J. Anti-angiogenic treatment (Bevacizumab) improves the responsiveness of photodynamic therapy in colorectal cancer. *Photodiagnosis and photodynamic therapy* **2018**, *23*, 111−118.
(43) Kragh-Hansen, U. Structure and ligand binding properties of human serum albumin. *Dan. Med. Bull.* **1990**, *37*, 57−84.
(44) Naczynski, D. J.; Andelman, T.; Pal, D.; Chen, S.; Riman, R. E.; Roth, C. M.; Moghe, P. V. Albumin nanoshell encapsulation of near-infrared-excitable rare-Earth nanoparticles enhances biocompatibility and enables targeted cell imaging. *Small (Weinheim an der Bergstrasse, Germany)* **2010**, *6*, 1631−1640.
(45) Surcel, M.; Constantin, C.; Caruntu, C.; Zurac, S.; Neagu, M. Inflammatory Cytokine Pattern Is Sex-Dependent in Mouse Cutaneous Melanoma Experimental Model. *J. Immunol. Res.* **2017**, *2017*, No. 9212134.
(46) Hill, G. J., 2nd; Moss, S. E.; Golomb, F. M.; Grage, T. B.; Fletcher, W. S.; Minton, J. P.; Krementz, E. T. DTIC and combination therapy for melanoma: III. DTIC (NSC 45388) Surgical Adjuvant Study COG PROTOCOL 7040. *Cancer* **1981**, *47*, 2556−2562.
(47) Tian, R.; Zeng, Q.; Zhu, S.; Lau, J.; Chandra, S.; Ertsey, R.; Hettie, K. S.; Teraphongphom, T.; Hu, Z.; Niu, G.; Kiesewetter, D. O.; Sun, H.; Zhang, X.; Antaris, A. L.; Brooks, B. R.; Chen, X. Albumin-chaperoned cyanine dye yields superbright NIR-II fluorophore with enhanced pharmacokinetics. *Sci. Adv.* **2019**, *5*, No. eaaw0672.
(48) Hu, S.; Dong, C.; Wang, J.; Liu, K.; Zhou, Q.; Xiang, J.; Zhou, Z.; Liu, F.; Shen, Y. Assemblies of indocyanine green and chemotherapeutic drug to cure established tumors by synergistic chemo-photo therapy. *Journal of controlled release: official journal of the Controlled Release Society* **2020**, *324*, 250−259.
(49) Griffiths, G.; Gruenberg, J.; Marsh, M.; Wohlmann, J.; Jones, A. T.; Parton, R. G. Nanoparticle entry into cells; the cell biology weak link. *Advanced drug delivery reviews* **2022**, *188*, No. 114403.
(50) Zhang, X.; Huang, B.; Shen, Y.; Yang, C.; Huang, Z.; Huang, Y.; Xu, X.; Jiang, Y.; Sun, X.; Li, X.; Yan, M.; Zhao, C. Near infrared light triggered reactive oxygen species responsive nanoparticles for chemo-photodynamic combined therapy. *Journal of materials chemistry. B* **2018**, *6*, 2347−2357.
(51) Kashino, G.; Kobashigawa, S.; Uchikoshi, A.; Tamari, Y. VEGF affects mitochondrial ROS generation in glioma cells and acts as a radioresistance factor. *Radiation and environmental biophysics* **2023**, *62*, 213−220.
(52) Li, M.; Yin, L.; Wu, L.; Zhu, Y.; Wang, X. Paclitaxel inhibits proliferation and promotes apoptosis through regul ation ROS and endoplasmic reticulum stress in osteosarcoma cell. *Mol. Cell. Toxicol.* **2020**, *16*, 377−384.
(53) Wu, L.; Xie, W.; Li, Y.; Ni, Q.; Timashev, P.; Lyu, M.; Xia, L.; Zhang, Y.; Liu, L.; Yuan, Y.; Liang, X. J.; Zhang, Q. Biomimetic Nanocarriers Guide Extracellular ATP Homeostasis to Remodel Energy Metabolism for Activating Innate and Adaptive Immunity System. *Adv. Sci.* **2022**, *9*, No. e2105376.
(54) Feng, B.; Niu, Z.; Hou, B.; Zhou, L.; Li, Y.; Yu, H. Enhancing Triple Negative Breast Cancer Immunotherapy by ICG-Templated Self-Assembly of Paclitaxel Nanoparticles. *Adv. Funct. Mater.* **2020**, *30*, 1616.
(55) Chen, Q.; Chen, J.; Yang, Z.; Xu, J.; Xu, L.; Liang, C.; Han, X.; Liu, Z. Nanoparticle-Enhanced Radiotherapy to Trigger Robust Cancer Immunotherapy. *Adv. Mater.* **2019**, *31*, No. e1802228.
(56) Caligiuri, G. Mechanotransduction, immunoregulation, and metabolic functions of CD31 in cardiovascular pathophysiology. *Cardiovascular research* **2019**, *115*, 1425−1434.
(57) Schaaf, M. B.; Garg, A. D.; Agostinis, P. Defining the role of the tumor vasculature in antitumor immunity and immunotherapy. *Cell Death Dis.* **2018**, *9*, 115.
(58) Braeuer, R. R.; Watson, I. R.; Wu, C. J.; Mobley, A. K.; Kamiya, T.; Shoshan, E.; Bar-Eli, M. Why is melanoma so metastatic? *Pigment cell & melanoma research* **2014**, *27*, 19−36.

https://doi.org/10.1021/acsami.4c18469
ACS Appl. Mater. Interfaces XXXX, XXX, XXX−XXX